FEW-NANOMETER ELECTRO-MECHANICAL NANOTUBE SYSTEMS

Joshua Island

A thesis
in
The Department
of
Physics

Presented in Partial Fulfillment of the Requirements
For the Degree of Master of Science (Physics)
Concordia University
Montréal, Québec, Canada

September 2011

Concordia University
School of Graduate Studies

This is to certify that the thesis prepared

By: **Joshua Island**

Entitled: **Few-Nanometer Electro-Mechanical Nanotube Systems**

and submitted in partial fulfillment of the requirements for the degree of

Master of Science (Physics)

complies with the regulations of this University and meets the accepted standards with respect to originality and quality.

Signed by the final examining committee:

Dr. Calvin S. Kalman _____ Chair

Dr. Mariana Frank _____ Examiner

Dr. Valter Zazubovich _____ Examiner

Dr. Alexandre Champagne _____ Supervisor

Approved _____

Chair of Department or Graduate Program Director

_____ 20 _____ _____

Dean of Faculty

Abstract

Few-Nanometer Electro-Mechanical Nanotube Systems

Joshua Island

We demonstrate a procedure to fabricate few-nanometer sized electro-mechanical carbon nanotube systems (NEMS) and study their electro-mechanical properties via electron transport. To fabricate these devices we use a computer-aided nano-etching technique to create nanometer sized gaps ($3.8 - 70\ nm$) in suspended gold wires on top of carbon nanotubes (CNT). The technique is reproducible and was used to make several devices. The length scale of these NEMS is an order of magnitude shorter than previously studied nanotube systems and allows us to explore the regime of strong electron-vibron coupling.

We observe strong coupling between the electrons and two different vibrational modes of carbon nanotubes. In ultra-clean single-wall carbon nanotube (SWCNT) devices we observe a strong driving of the bending mode from charge transport with frequencies exceeding 600 GHz. In other devices we also measure a suppression in low-bias voltage due to a strong coupling between electrons and the longitudinal stretching mode (Franck-Condon Effect). We extract a coupling factor of ($g = 2.2 \pm 0.4$), among the largest seen in suspended nanotube devices. We measure vibrational modes up to 9 THz in these NEMS.

Acknowledgments

I would like to acknowledge those who have made this thesis and my short stay here in Montreal possible.

To my supervisor, Alex, I thank you for your knowledge and dedication but more than this I thank you for your enthusiasm. Where there was once a flame of interest now burns a wildfire of passion that I will carry on in my career.

To Vahid, my friend and colleague, thank you for your patience and kindness. Your humor is a much valued thing in the long lab hours. I would like to thank Andrew, my friend at first sight, for helping me during this summer. I wish you great success in the devices to come. Serap, I thank you for your help in preparing my thesis and paving the way in the Champagne Group. Jimi, Matt, and Roopak, you made the lab a fun place to be. Thanks for your help and support, good luck to you all.

I would like to thank my parents and brother for teaching me the value of education and that learning should have no end.

Finally, to my dearest wife Jade whom I have made wait far, far too long, you've been a great source of motivation and support for me. I'll be home soon.

Contents

List of Figures

List of Tables

Chapter 1

Introduction

The coupling of electronics and mechanics becomes stronger as the size of an electromechanical system becomes smaller. At the nanoscale this coupling is large enough to offer a fundamental study of the physics behind the influence of mechanics on electronics and vice-versa. Nanoelectromechanical systems (NEMS) are a platform for this study and have applications as sensitive sensors [1, 2, 3]. Carbon nanotubes are a novel material with unique electrical and mechanical properties which have made them popular for studying the physics of one dimensional and zero dimensional systems [4]. A carbon nanotube is a rolled up hexagonal framework of carbon atoms that forms a hollow tube with a diameter of a few nanometers [5].

In this thesis we demonstrate a procedure to fabricate few-nanometer sized electromechanical carbon nanotube systems (NEMS) and study the coupling between their electronics and mechanics. To fabricate these devices we use a computer-aided nanoetching technique to create nanometer sized gaps ($3.8 - 70nm$) in suspended gold

wires on top of carbon nanotubes. We coded software based on a feedback system to controllably etch the gold wires to create few-nanometer gaps. We further developed this process to make larger gaps by breaking the gold wires at selected powers. The device shown in Fig. 1.1**a.** was etched down and then broken at a power of 20 mW to create a gap of ≈ 70 nm. This technique is reproducible and was used to make several devices. The length scale of the smallest of these NEMS (down to 3.8 nm shown in Fig. 1.1**b.**) is an order of magnitude shorter than previously studied nanotube systems and allows us to explore the regime of strong electron-vibron coupling.

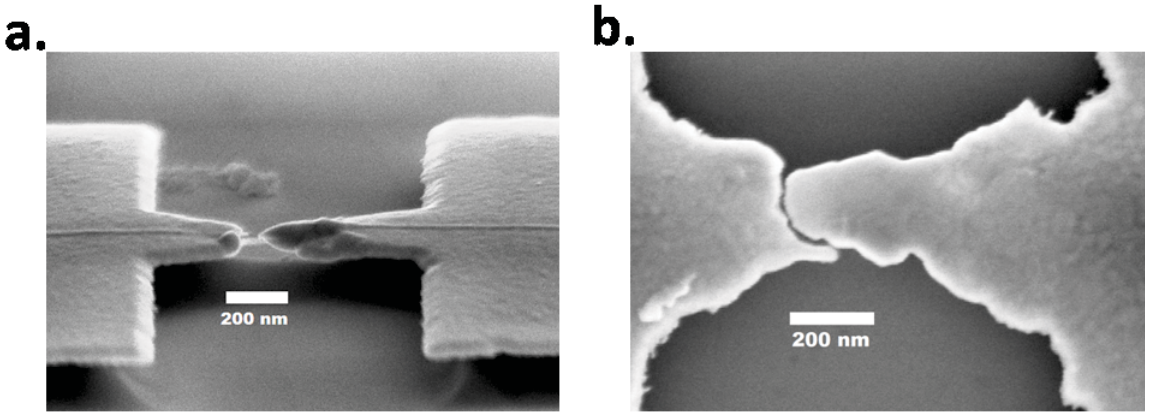

Figure 1.1: SEM image of gaps formed in two breakjunctions by electromigration. **a.** A gap of ≈ 70 nm was created by first controllably etching the junction and then breaking it at 20 mW power. **b.** A smaller gap of just 3.8 nm (from Data, see Chapter 5) was created by breaking the junction at a lower power.

We observe strong coupling between the electrons and two different vibrational modes of carbon nanotubes in 3 devices. In ultra-clean carbon nanotube devices we observe a strong driving of the bending mode from charge transport with frequencies exceeding 600 GHz. In other devices we also measure a suppression in low-bias voltage due to

a strong coupling between electrons and the longitudinal stretching mode (Franck-Condon Effect). We extract a coupling factor of ($g = 2.2 \pm 0.4$), among the largest seen in suspended nanotube devices [6, 7]. We measure vibrational modes up to 9 THz in these NEMS.

In chapter 2 we review some of the basic theory of carbon nanotubes in one and zero dimensions. Single electron transistor (SET) theory is discussed with an emphasis on the coupling of electrons and vibrons. In chapter 3 we cover the fabrication of devices such as the one shown in 1.1 up to the gap creation process. The chapter finishes with a brief presentation of the instrumentation and software used to make our measurements. The nano-etching process (electromigration) is reviewed in chapter 4. The few-nanometer gap creation process is explained as well as the controlled power break method. The chapter ends with a note on the other applications of the gap creation process with respect to graphene and other materials. In chapter 5 we present the results for devices showing coupling between electrons and the longitudinal vibrational mode and a device showing coupling between electrons and the bending mode of a SWCNT.

Chapter 2

SWCNT: from 1D to 0D

The unique properties of nanotubes make them a strong candidate for a study of the coupling between electronics and mechanics. The first measurements on single-wall carbon nanotubes (SWCNTs) in a transistor configuration were done in 1997 about six years after their discovery [8]. Later in 2004, suspended nanotube devices were fabricated to create a resonator capable of self oscillatory detection [3]. Then in 2006, the connection was made between the electrical transport and mechanical motion of a suspended single-wall carbon nanotube quantum dot (QD) [6]. In this chapter we review these electrical and mechanical properties and how they become intertwined at the nanoscale. We go from a one dimensional nanotube conductor to a zero dimensional one where the coupling is detectable through electron transport. The two parameters which determine the one dimensional behavior or the zero dimensional behavior are the size of the device (length of the tube) and the contact resistance to the tube. Quantum effects become apparent when the size of the device becomes

comparable to the scattering length of carriers in the tube. Devices in this regime with poor contacts show zero dimensional behavior while those with good contacts have high conductances with nearly no scattering (ballistic conductance). We first derive the energy band structure of a SWCNT starting from the band structure of graphene (a single layer of carbon atoms).

Graphene is a honeycomb lattice of carbon atoms, see Fig. 2.1. Each carbon atom has four valence electrons. Three of these are used to make in-plane carbon-carbon bonds to create the lattice (sp_2 bonding). The last is a free electron in the $2p_z$ orbital and is responsible for electronic conduction. Wallace first derived the band structure for graphene in 1947 [9] using the tight binding approximation [10]. In the tight binding approximation, the electronic wavefunction is constructed as a superposition of the atomic orbitals of the lattice and satisfies Bloch periodicity. Graphene has a two-atom basis, which can be described as two inter-penetrating hexagonal lattices, so the total wavefunction is the sum of the superpositions for each sub-lattice,

$$\psi(\vec{r}) = \sum_1 exp[2\pi i\vec{k}\cdot\vec{r}_1]X(\vec{r}-\vec{r}_1) + \lambda\sum_2 exp[2\pi i\vec{k}\cdot\vec{r}_2]X(\vec{r}-\vec{r}_2) \qquad (2.1)$$

where X is the normalized $2p_z$ orbital with periodicity of the lattice and the sum for atoms 1 and 2 is taken over all lattice points and λ is the phase factor between the two atoms. Through the Schrodinger equation we then find the eigenenergy. The valence and conduction bands of graphene are given by,

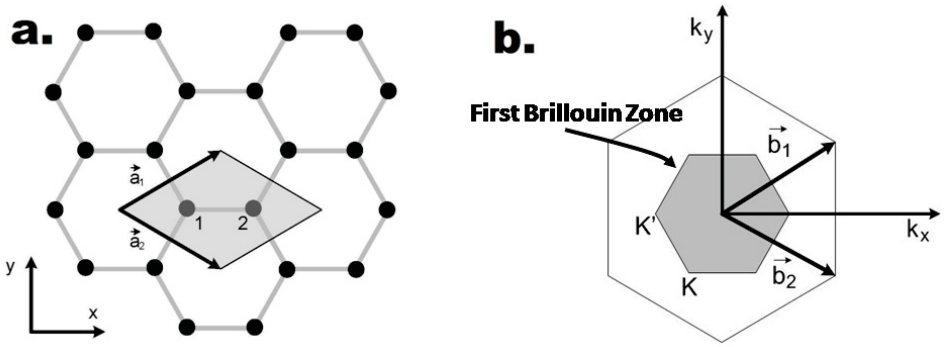

Figure 2.1: **a.** Real space graphene lattice with primitive vectors $\vec{a}_1$ and $\vec{a}_2$. The lattice has a two atom basis, labeled 1 and 2 **b.** Reciprocal lattice with shaded first Brillouin zone and primitive vectors $\vec{b}_1$ and $\vec{b}_2$.

$$E(k_x, k_y) = \pm\gamma\sqrt{1 + 4cos^2\left(\frac{k_x a}{2}\right) + 4cos\left(\frac{\sqrt{3}k_y a}{2}\right)cos\left(\frac{k_x a}{2}\right)} \tag{2.2}$$

where γ is the hopping integral, or transfer integral from the tight binding approximation, $a = 2.49\mathring{A} = |\vec{a}_1|, |\vec{a}_2|$ is the magnitude of the primitive vectors in Fig. 2.1a., and k_x, k_y are the magnitudes of the wavevectors.

If we look at the energy around the Dirac points, the points at each corner of the Brillouin zone, K, K', in Fig. 2.1**b**, we find a degeneracy. At low energies, the dispersion relation is linear in $\vec{k}$, the crystal momentum.

$$E(\vec{k}) \approx \pm\hbar v_F|\vec{k}| \tag{2.3}$$

where $v_F \approx 10^6 m/s$ is the Fermi velocity of electrons in graphene. Through this relation we see that the holes and electrons near this point behave relativistically and

can be described by the Dirac equation. The K, K' points give rise to a degeneracy called valley or iso-spin degeneracy. From the band structure of graphene we can construct that of a SWCNT.

A SWCNT is a graphene sheet that has been wrapped up to form a cylinder. There are many ways to wrap up a graphene sheet and the wrapping determines what type of tube will result. The classifications of nanotubes that are based on the wrapping of a vector, $\vec{C}_h$ shown in Fig. 2.2, defined on the graphene sheet. The wrapping vector is related to the real space primitive vectors through a set of wrapping indices (n, m).

$$\vec{C}_h = n\vec{a}_1 + m\vec{a}_2 \tag{2.4}$$

The three classes of tubes are armchair, zigzag and chiral. Zigzag tubes have $m = 0$ and are called so because the carbon atoms "zigzag" along the wrapping vector. Wrapping vectors that fall on the zig-zag dotted line in Fig. 2.2 create zig-zag tubes. Armchair tubes have $n = m$ and the atoms form "chairs" along the wrapping vector. Wrapping vectors that fall on the armchair dotted line in Fig. 2.2 create armchair tubes. All other wrapping indices form chiral tubes where the wrapping vector falls in between the zig-zag and armchair lines. The wrapping vector defines the perpendicular axis of the tube and the translational vector, $\vec{T}$ in Fig. 2.2, defines the tube axis.

The wrapping of the graphene sheet creates a restriction on the perpendicular wavevector, $\vec{k}_\perp$, of electrons which is in the same direction as $\vec{C}_h$ in Fig. 2.2.

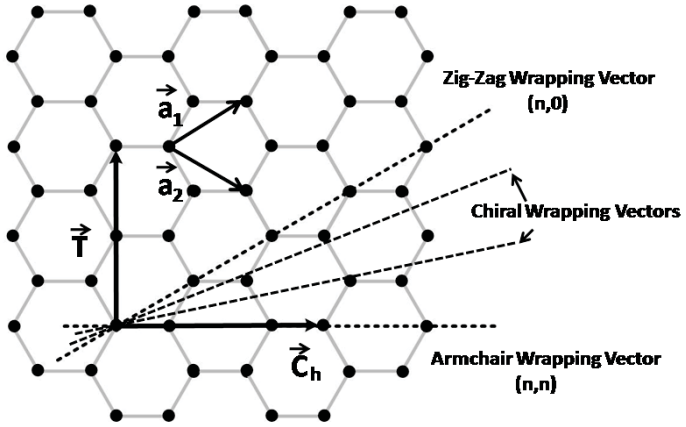

Figure 2.2: The wrapping vector $\vec{C}_h$ defines the type of tube. The dotted lines mark the vectors at which the tube will be zig-zag or armchair. If the vector lies in between these it will be a chiral tube. The translation vector $\vec{T}$ defines the tube axis.

The wavevector must be single valued around the tube circumference so it becomes quantized in this direction, taking on values according to the boundary conditions on the plane wave portion of the electron wavefunction.

$$e^{i\vec{k}\cdot\vec{r}} = e^{i\vec{k}\cdot(\vec{r}+\vec{C}_h)} \tag{2.5}$$

These boundary conditions quantize the perpendicular wavevector in the following way,

$$\vec{k}\cdot\vec{C}_h = 2\pi p \Rightarrow d\pi k_\perp = 2\pi p \tag{2.6}$$

where d is the tube diameter and p is an integer that labels the energy sub-bands. This quantization corresponds to 1D cuts in the graphene band structure, where each

1D sub-band is spaced by a perpendicular wavevector quantization of $2/d$. Depending on where this 1D sub-band cuts the Brillouin zone in Fig. 2.3**a.**, the nanotube can be metallic or semiconducting. If the sub-band runs directly through the Dirac point, at the degeneracy in Fig. 2.3**b.**, then the valence and conductance bands of the nanotube meet and form a metallic tube. Higher sub-bands for a metallic tube cut the sides of the cone and have a band gap shown in Fig. 2.3**c.**. If the allowed sub-bands do not run through the center of the dispersion cone then there is a gap between the valence and conductance bands for all sub-bands making a semiconducting tube. The class of metallic tubes include armchair tubes which have zero bandgap and small bandgap tubes which have bandgaps $< 100mV$ [4]. Small bandgap tubes have $2n + m$ equal to a multiple of 3 [11]. Zig-zag tubes are semiconducting.

Let us now look at a specific example for an armchair tube with indices $(n, m) = (n, n)$. We can relate $\vec{k}_\perp$ to the reciprocal space wavevectors in the following way,

$$\vec{k}_\perp = \frac{[(2n+m)\vec{b}_1 + (2m+n)\vec{b}_2]}{2(m^2+nm+n^2)} = \frac{\vec{b}_1 + \vec{b}_2}{2n} = \frac{1}{2n}\frac{4}{\sqrt{3}a}\vec{k}_x \tag{2.7}$$

where $\vec{b}_1, \vec{b}_2$ are the vectors shown in Fig. 2.1**b**. The allowed values of the above are integer multiples of this result where the integer runs from $-n$ to n. Upon substitution of this into Eq. 2.8 we have the band structure for an armchair tube,

$$E(k_y, p) = \pm\gamma\sqrt{1 + 4cos^2\left(\frac{k_y a}{2}\right) + 4cos\left(\frac{k_y a}{2}\right)cos\left(\frac{\pi p}{n}\right)} \tag{2.8}$$

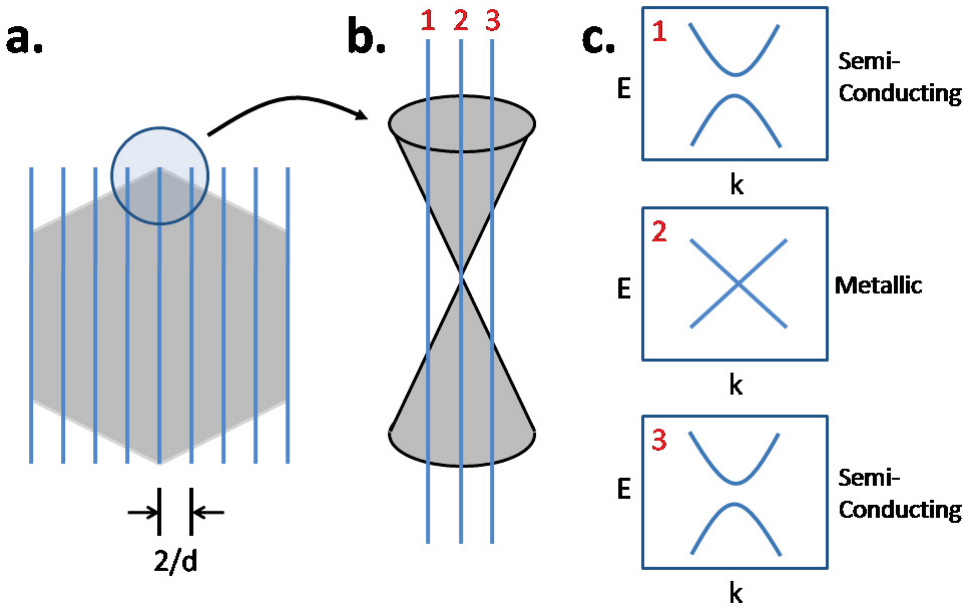

Figure 2.3: Allowed subbands of a metallic nanotube. The sub-bands cut the dispersion cone at different positions. The example graphs give a qualitative idea of what the dispersion relation looks like for each subband.

where p is the integer from $-n$ to n defining the sub-bands of the armchair nanotube and k_y is parallel to the tube axis. We plot the function for a $(3,3)$ armchair nanotube in Fig. 2.4. The $(3,3)$ armchair tube is one of the smallest stable single wall tubes possible with a diameter of 0.41 $\mathring{A}$ [12]. Examples for other tubes can be found in [13].

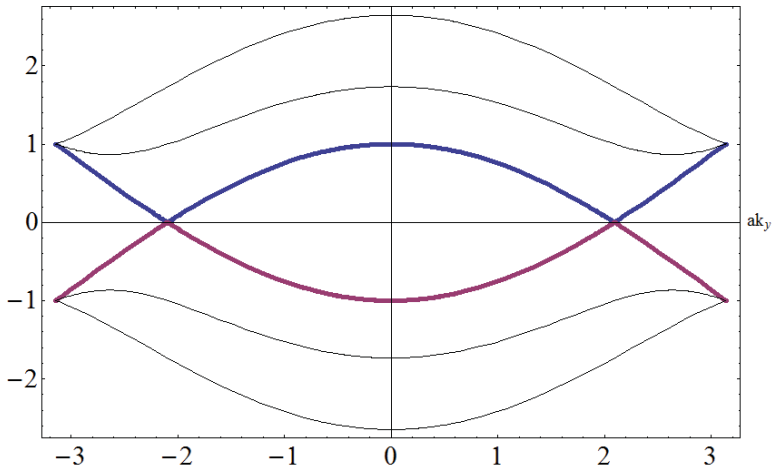

Figure 2.4: Energy band plot for a $(3,3)$ armchair nanotube. The conduction band (blue, upper curve) and valence band (purple, lower curve) meet forming a metallic tube. Near the meeting points (Dirac points) the dispersion relation is linear in k_y. Higher energy bands are in plotted in black.

2.1 SWCNT as One Dimensional Systems

2.1.1 Electron Transport

Electron transport in 1D nanotubes is described by the Landauer formula, Eq. 2.9 [14]. Nanotubes have four conducting channels owing to the spin and iso-spin degeneracy of their electronic sub-bands. Each channel gives a maximum conductance

of e^2/h. Neglecting temperature effects the conductance is given by,

$$G = \frac{4e^2}{h} \sum_i T_i(E_f) \tag{2.9}$$

where $T_i(E_f)$ is the transmission probability of the i^{th} sub-band at the Fermi energy, E_f. In the diffusive regime the conductance scales with the mean free path (MFP), l which is the distance between scattering events of charge carriers in the tube, when l is shorter than the device length, L,

$$G = \frac{4e^2}{h} \frac{l}{l+L} \qquad , \qquad l \ll L \tag{2.10}$$

When the device is shorter than the mean free path, as in our ultra-short tubes, the electrons have perfect transmission and the device enters the ballistic regime. In this regime the full quantized conductance for the sub-band can be realized and the conductance is close to $G = 4e^2/h$. [4, 15]

From the conductance of the device we can calculate the carrier mobility which is a measure of how fast the carriers move through the tube. It also reflects the "cleanliness" of the device.

$$\mu = \frac{\sigma}{ne} = \frac{dG}{dV_g} \frac{L}{C'} \qquad , \qquad C' = \frac{C}{L} \tag{2.11}$$

where σ is the conductivity, e is the electron charge, n is the number of carriers, V_g is the gate voltage, and L is the length of the device. In Fig. 2.5 we have used Eq. 2.11 to plot the mobility of a semiconducting tube given the current as a function of gate voltage. The mobility for this nanotube reaches more than 7000 cm^2/Vs.

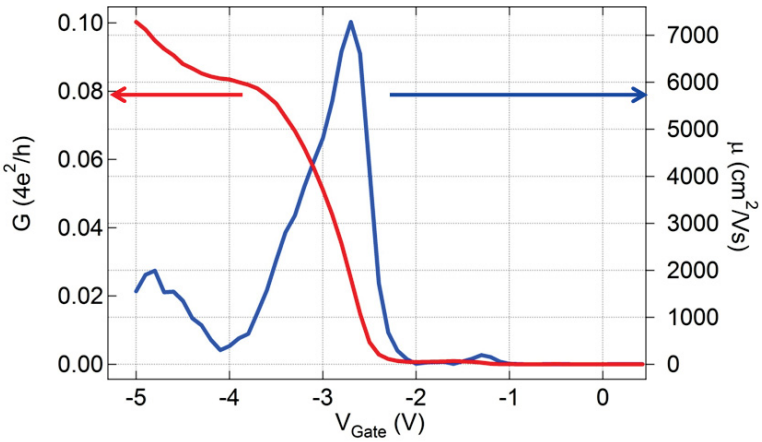

Figure 2.5: Mobility and conductance of a semiconducting nanotube plotted against the gate voltage.

If we model the nanotube as a conducting wire parallel to a conducting wall (gate electrode), then the capacitance is

$$\frac{C}{L} = \frac{2\pi\epsilon}{ln(\frac{d}{a} + \sqrt{\frac{d^2}{a^2} - 1})} \tag{2.12}$$

where d is the distance to the wall, a is the radius of the tube, $\epsilon = \epsilon_r\epsilon_0$ is the product of the dielectric constant and permittivity of free space.

2.2 Between 1D and 0D

Here, we briefly mention the transitions from the one dimensional (high transmission) behavior to the zero dimensional (low transmission) quantum behavior of a SWCNT. When the tunneling barriers become more reflective and the conductance decreases to $\approx 2e^2/h$, the device becomes an electron waveguide where electrons scatter off the barriers of the device and interfere in the nanotube, termed Fabry-Perot interference [16, 17]. With more scattering and an average conductance near e^2/h, the device displays higher ordered tunneling processes such as cotunneling as well as the Kondo effect, more on these can be found in [18].

2.3 SWCNT as Zero Dimensional Systems

When we contact a ballistic nanotube via tunneling barriers we confine the carriers to a short tube section and create a small conducting island. The confinement sets up quantized charge states on the island which carriers can tunnel in and out of. Poor wetting between the tube and contacts, or more importantly Schottky barriers, can create such tunnel barriers to the tube. In the case of Schottky barriers the alignment of the Fermi level of the contacts inside the bandgap of the nanotube creates a tunneling barrier for carriers as shown in Fig. 2.6. The barrier for holes or electrons may be different if the Fermi levels do not align to the center of the nanotube bandgap.

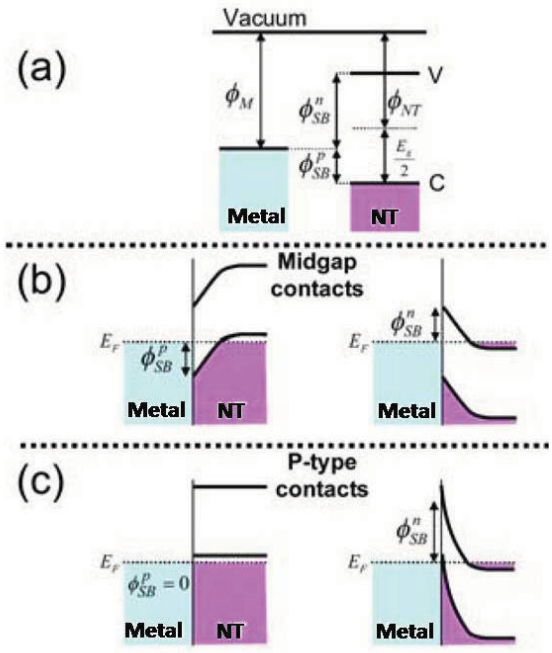

Figure 2.6: **a.** Schottky barrier formed between a metallic contact and a semiconducting carbon nanotube. **b.** Alignment of the contact's Fermi level with the midgap of the nanotube **c.** p-type band alignment. Adapted from Biercuk et al.

In the case of a p-doped tube alignment in Fig. 2.6**c.**, holes have essentially no barrier whereas electrons have a barrier equal to the size of the tube bandgap. The Schottky barrier can be calculated given the work functions for the metal and tube, ϕ_M, ϕ_{NT} respectively, and the bandgap, E_g.

$$\phi^p_{SB} = \phi_{NT} + E_g/2 - \phi_M, \qquad \phi^n_{SB} = \phi_M + E_g/2 - \phi_{NT} \tag{2.13}$$

2.3.1 Single Electron Transistors (SET)

In this section we describe the basic properties of a single electron transistor (SET) needed to understand electron transport in our ultra-short nanotube devices. Single electron transistor theory has been thoroughly reviewed by several papers [19, 20, 21, 22]. In our devices, tunnel barriers between the nanotube and the source and drain electrodes create a conducting island that is capacitively coupled to the three electrodes. A model of the capacitive coupling to the source, drain, and gate is shown in Fig. 2.7. The capacitive coupling to the gate allows the adjustment of the electrostatic potential on the dot. Electrons that tunnel on the dot must overcome a charging energy set by the coulomb repulsion from the electrons on the dot and have sufficient energy to enter an available state. We will see later how the charging energy and level spacing can block the current through the transistor for certain configurations of bias and gate voltages, this effect is aptly named Coulomb Blockade. We start by looking at a dot in its ground charge states and then consider its excited states.

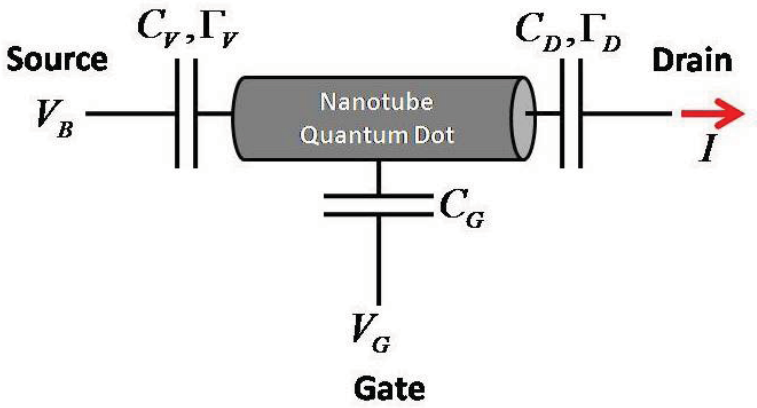

Figure 2.7: Schematic of nanotube quantum dot. The dot is capacitively connected to three electrodes. The source and drain are tunnel barriers with tunnel rates of Γ_S and Γ_D, respectively.

2.3.2 Charge States

The complete discrete spectrum of states on the dot is a combination of the charging energy (E_C) and the quantum single particle energy states. The charging energy arises from the classical energy required to charge a capacitor. The single particle state energies are a result of the confinement of electrons on the dot. The energy spacing between two levels is δ. To add an electron to the dot, a maximum total energy of $E_C + \delta$ is required. If we assume that the charging energy and capacitances are independent of the number of electrons on the dot, then the total energy of the dot with N electrons is given by a sum of the total energy from the quantum levels, capacitive charging energy of the dot, and the total dot potential,

$$U(N) = \sum_{N=1}^{N} E_i + \frac{(Ne)^2}{2C} + NeV \tag{2.14}$$

where $C = C_g + C_s + C_d$ is the total capacitance and $V = \frac{C_s V_s + C_g V_g}{C}$ is the total dot potential since the drain voltage (V_d) is zero (grounded) in our experiments and does not contribute to the total. The energy required to add the Nth electron to the dot is given by the electrochemical potential, or the difference in the energy of the dot with N electrons and N-1 electrons.

$$\mu_N = U(N) - U(N-1) = (2N-1)E_C + \delta_N - eV \tag{2.15}$$

The term $E_C = e^2/2C$ is the charging energy. The difference in the chemical potential of the N state and N-1 state defines the addition energy, $E_C + \delta$, and is the level spacing shown in a model for the energy levels of the system in Fig. 2.8 as can be seen by setting $N = 1$ and $V = 0$ in Eq. 2.15.

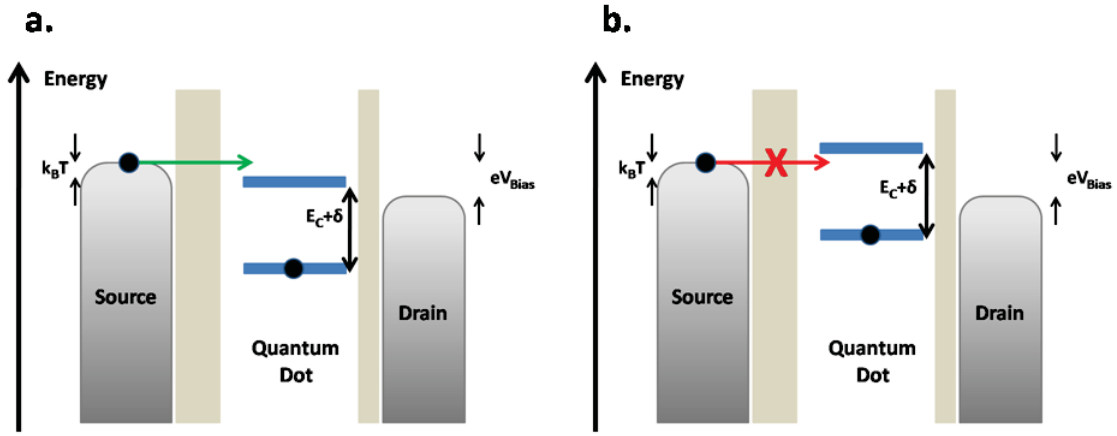

Figure 2.8: Energy level diagram for a quantum dot. **a.** The current flows as electrons sequentially tunnel on and off the dot. **b.** The current is blocked because electrons cannot tunnel onto the dot as there is no available charge state in the bias window, eV_{bias}.

A charge state must lie within the bias window, eV_{Bias}, which is the difference between the source and drain Fermi levels, for current to flow (see Fig. 2.8). In Fig. 2.8**a.** electrons tunnel onto the dot through the source tunnel barrier to occupy the charge state on the dot and then tunnel off through the drain tunnel barrier. If no charge state lies within the bias window, an electron cannot tunnel onto the dot and the current is blocked as in Fig. 2.8**b.**. Fig. 2.9 shows the various tunneling thresholds that correspond to this blockade in a 2D plot of the I vs. V_{bias}, V_{gate}.

The central white diamond in Fig. 2.9**a.** is Coulomb blockade (no current flows) and corresponds to the dot having N electrons in its ground state. The side diamonds represent the dot with N-1 electrons (left) and N+1 electrons (right) in its ground state. Each edge of the diamond (labeled b, c, d, e in Fig. 2.9) are thresholds at which current flows for the N electron state. The band alignments for the four thresholds are shown in Fig. 2.9. Labels **b.** and **c.** are the positive bias voltage edges where the charge state aligns with the source in **b.** and the drain in **c.**. Labels **d.** and **e.** are the negative bias edges where the charge state aligns with the source in **d.** and the drain in **e.**. From the slopes of the current thresholds in Fig. 2.9**a.** the capacitances for the device can be extracted. It's possible for δ to be zero due to the four-fold degeneracy found in CNTs.

2.3.3 Electronic Excited States

We are now ready to consider excited quantum states. For simplicity, let us consider two excited states with N electrons as shown in Fig. 2.10 as dotted lines. The occupied

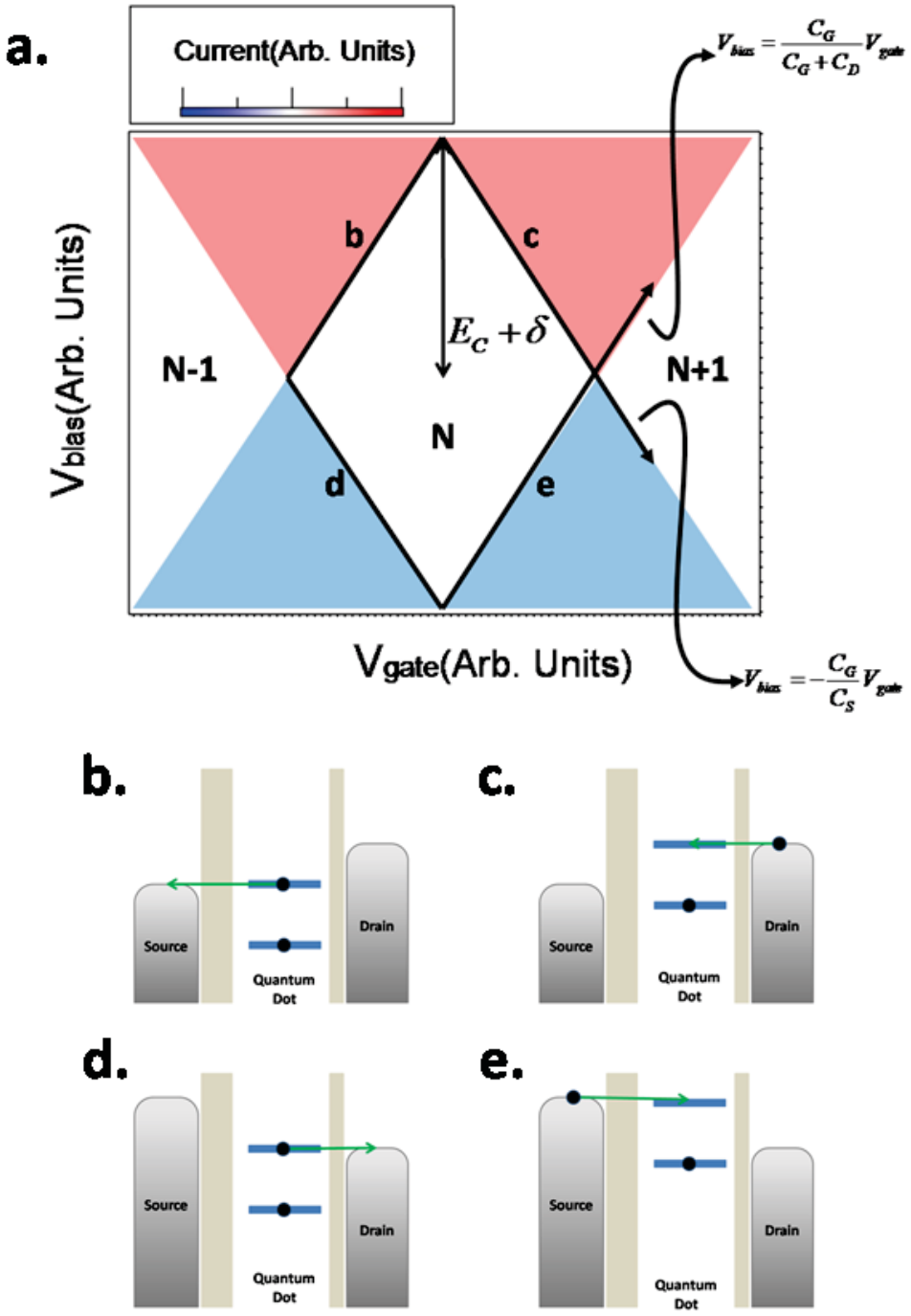

Figure 2.9: Cartoon of a 2D contour plot. The current is plotted vs. the bias and gate voltages. The addition energy $E_C + \delta$ is the height of the diamond. The four tunneling thresholds, labeled **a.** to **d.** correspond to the energy diagrams. The source aligns with the charge state in **a.** and **d.**. The drain aligns with the charge state in **b.** and **c.**. The capacitance ratios for the device can be extracted from the slopes of the tunneling thresholds.

(unoccupied) levels correspond to having N (N-1) electrons. The energy spacing for the excited states is δ. An electronic state must lie in the bias window to have current flow. If both a ground state and an excited state fall in the bias window then there are two available states for electrons to tunnel to which increases the overall current (proportional to the density of available states as given by Fermi's Golden Rule).

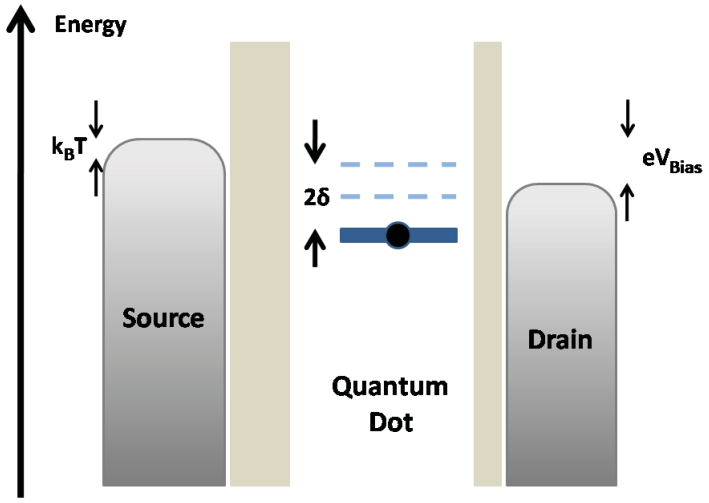

Figure 2.10: Energy level diagram for a quantum dot allowing for excited states. The charge addition energy is $E_C + \delta$

We draw a 2D plot in Fig. 2.11 of the current voltage characteristics which details the transport across the dot of Fig. 2.10. This time two steps are found in the triangular conducting regions. At the four positions, a, b, c, d, in Fig. 2.11 the two excited states for the N-1 ground state align with the source or drain. At position **a** (**d**) the second excited state aligns with the source (drain). At position **b** (**c**) the first excited state aligns with the drain (source). Here we have only considered two excited states

for the N-1 ground state but in actuality there exists higher electronic excited states and the level spacing δ may not be constant. By varying the bias and gate voltages we can probe the out of equilibrium states for the system.

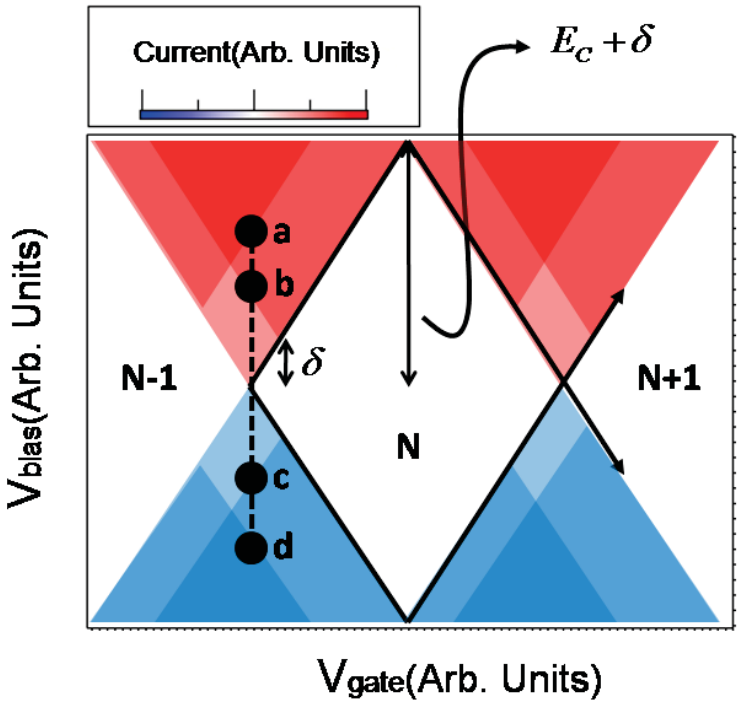

Figure 2.11: Cartoon 2D plot of a quantum dot with excited states. The four positions indicate when the excited states align with the drain or source. At position **a** (**d**) the N-1 excited state aligns with the source (drain). At position **b** (**c**) the N excited state aligns with the drain (source).

2.3.4 Vibronic Excited States

A suspended quantum dot has a vibrational energy spectrum which adds to the electronic energy levels we just discussed. Suspended nanotube quantum dots can be described by the Anderson-Holstein model. The electronic portion of the total

Hamiltonian for the system includes a vibronic term which is a result of the coupling between electrons and vibrons (quantized vibrational states),

$$H_{el} = \sum_{s=\uparrow,\downarrow} \sum_{s=\nu,q} [\epsilon + \lambda_q^{(\nu)} \hbar\omega_q^{(\nu)} (b_q^{(\nu)\dagger} + b_q^{(\nu)})^j] n_s + E_C n_\uparrow n_\downarrow, \tag{2.16}$$

where ϵ is the single particle electronic energies, E_C is the charging energy, n_s is the electron number operator (with spin s), and $b_q^{(\nu)}$ ($b_q^{(\nu)\dagger}$) is the annihilation (creation) operator for a vibron of energy $\hbar\omega$, wave number q, and mode ν (Stretching, twisting, breathing, bending, see end of chapter). The coupling constant, λ, gives the strength of the coupling and is mode dependent. The interaction can be linear ($j = 1$) or quadratic ($j = 2$) [23].

The total wavefunction of the QD is a combination of the electronic wavefunction and the vibronic wavefunction for the system.

$$\Psi_{dot} = \psi_{elec} \psi_{vib} \tag{2.17}$$

When an electron tunnels onto the dot, it changes the vibronic portion of the total wavefunction. The probability for the tunneling event to occur is given by the overlap of the total wavefunction before and after tunneling.

$$P = |\langle \Psi_{after} | \Psi_{before} \rangle|^2 \tag{2.18}$$

In the case of large coupling, shown in Fig. 2.12**a.**, the vibronic wavefunction is greatly affected and the overlap for the higher vibronic excited states is greater than for the ground state, thus the electron must excite a vibron to tunnel on the dot. In the case of weak coupling, shown in Fig. 2.12**b.**, the vibronic wavefunction is barely modified and the overlap of the vibronic ground states is large such that an electron does not have to excite a vibron to tunnel on the dot.

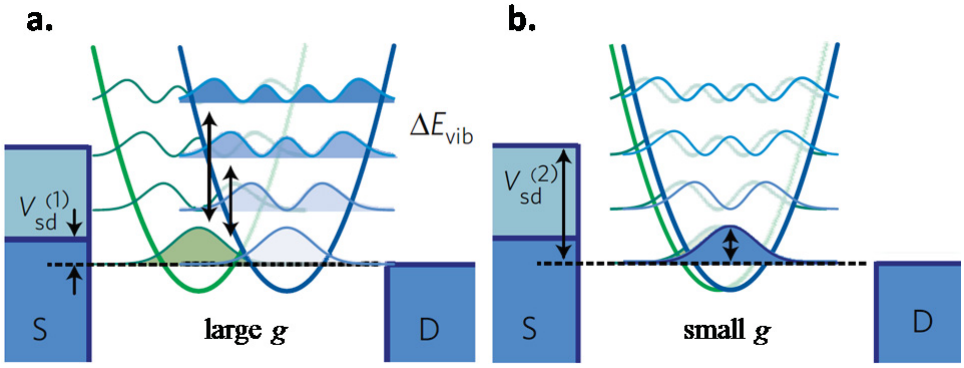

Figure 2.12: Overlap of the vibronic wavefunction before and after the electron tunnels onto the dot. **a.** For a tunneling event with strong coupling, large g, the overlap of excited vibronic states is more than the one for the ground states. **b.** For a tunneling event with weak coupling, small g, the overlap of the ground states is more than for excited states. Adapted from Leturcq et al.

Large coupling leads to a blockade in current at low biases. This is called the Franck-Condon blockade and it is more thoroughly reviewed in [6, 7, 23, 24]. The vibronic overlap is proportional to the height if the differential conductance (dI/dV) peaks,

$$\left(\frac{dI_{sd}}{dV_{sd}}\right)_n^{max} \propto |M_{0\to n}|^2 \propto \frac{e^{-g}g^n}{n!} \tag{2.19}$$

where $|M_{0\to n}|^2$ is the probability to excite n vibrons starting from the ground state. The coupling factor g, tells us the strength of the e-v coupling [25]. This coupling factor is related to the coupling constant λ in Eq. 2.16 by $g = \lambda^2$. We can thus probe these excited vibronic states much in the same way as was described in the previous section by varying the bias and gate voltages and measuring their energy position in a 2D plot. Then from Eq. 2.19 we can extract the coupling strength of the device.

In carbon nanotubes there are a number of low energy acoustic vibrational modes that the electron could couple to. The tube can bend, breath, stretch, and twist, as shown in Fig. 2.13. It has been shown that of these modes the electrons couple strongly to the stretching and breathing modes by inducing a scalar deformation potential while the others couple through modification of the hopping integral from changes in the C-C bond lengths (vector potential) and couple less strongly [23]. The bending mode (out of plane mode) is a special case where the electron-vibron coupling can be increased by a positive feedback when the tube is driven on resonance [26, 27]. This mode appears in devices with high quality factors (low dissipation oscillator). When electrons tunnel at a rate greater than the resonance frequency for the bending mode it can drive the bending mode on resonance. With a high quality factor the vibration from one tunneling event can last until the next event. This increases the coupling factor g (due to the electric dipole moment) and the next electron is more likely to excite the mode again thus starting a positive feedback.

The energies for these modes scale with the length of the tube in different ways except

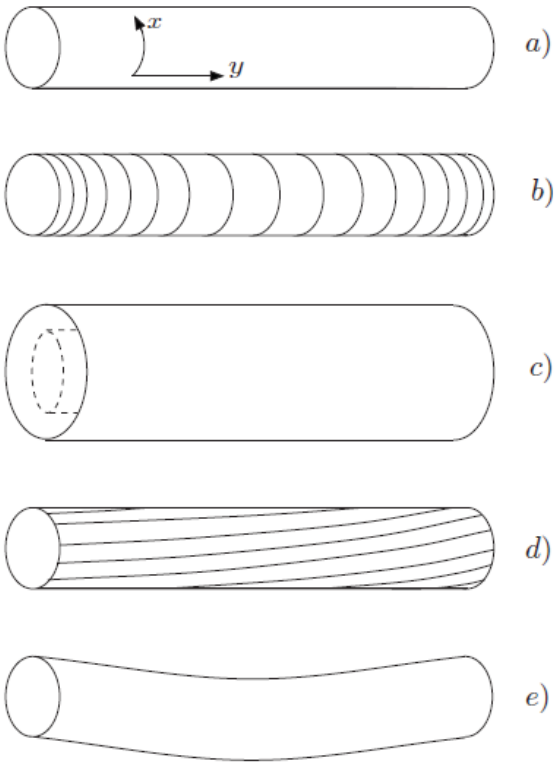

Figure 2.13: **a.** Stationary tube. **b.** Stretching or longitudinal mode. **c.** Breathing mode. **d.** Twisting mode. **e.** Bending mode. Adapted from Mariani et al.

for the breathing mode which is length independent. In Fig. 2.14 we plot the energy vs. length of each vibrational mode.

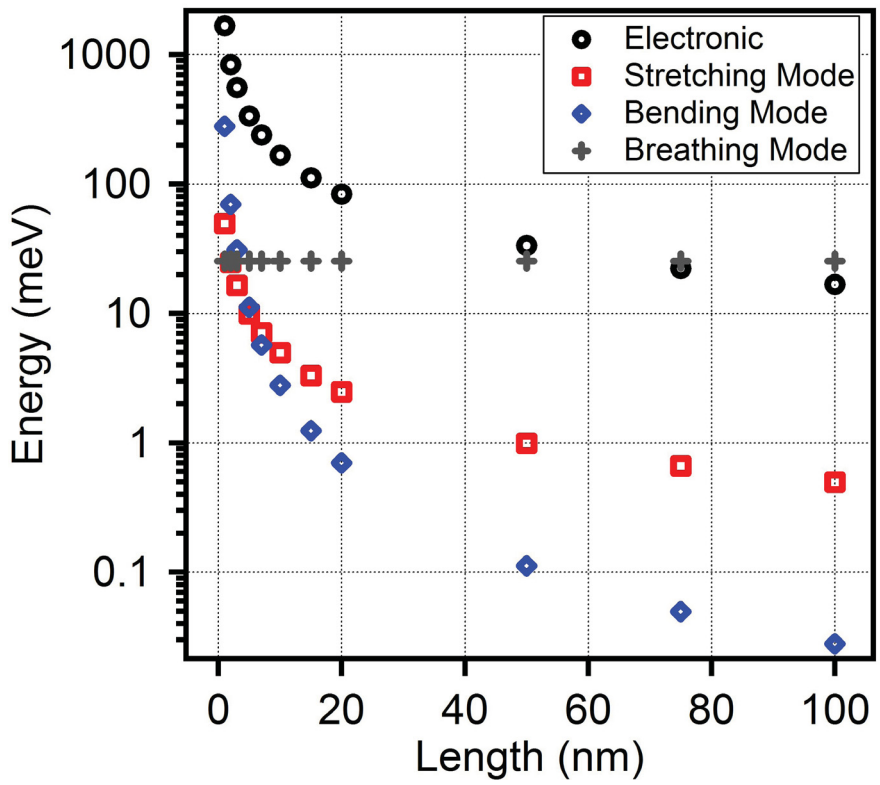

Figure 2.14: Vibronic and electronic energies versus length of tube. The tube diameter is 1.1 nm for the breathing mode.

The excitation energy of the stretching mode is given by,

$$E_s = \hbar v_{ph} q \tag{2.20}$$

where $v_{ph} \approx 2.4 \times 10^4$ is the acoustic phonon group velocity in nanotubes and $q = n\pi/L$, where n is the n^{th} mode and L is the length of the vibron. The breathing mode

energy is given by $E_b = 28\ meV/d(nm)$, where d is the tube diameter in nm [6]. The bending mode frequency is related to the length of the tube by the following,

$$f_{Bend} = \frac{22.4}{2\pi L^2} r \left(\frac{Y}{\rho}\right)^{\frac{1}{2}} \tag{2.21}$$

where r is the tube radius, $\rho = 1350\ kg/cm^3$ is the tube density, and $Y = 1.2\ TPa$ is Young's modulus [28]. The energy is then given by $E = hf_{Bend}$. The electronic excitations are plotted with the vibronic energies to give a comparison and for analysis in chapter 5. The electronic energies are given by

$$E_{elec} = hv_F/2L \tag{2.22}$$

where v_F is the Fermi velocity for electrons in the nanotube and L is the length of the tube.

Chapter 3

Device Fabrication and Instrumentation

3.1 Fabrication

In this chapter we describe the steps involved in fabricating our suspended single wall carbon nanotube (SWCNT) transistors and quantum dots (QDs). The majority of these steps are standard microfabrication procedures which we modified for our purpose. The difficulties of the device fabrication lie in the precise alignment and fabrication of gold bow-tie breakjunctions on top of nanotubes which will allow us to create few-nanometer long carbon nanotube (CNT) nanoelectromechanical systems (NEMS). This last step of few-nm gap formation will be described in chapter 4.

Figure 3.1 shows the geometry of our devices which forms a 3 terminal transistor. The gold bow-tie provides the source and drain electrodes and the silicon substrate,

above which the gold bridge is freely suspended, acts as a backgate electrode. The tube and junction are suspended to remove disorder due to the substrate. Moreover, the suspended tube is free to vibrate (NEMS). Suspension also minimizes heat leakage outside of the tube and makes it possible to anneal the tube at high temperature by flowing a large current (Joule Heating). The breakjunction (small gold bow-tie) at the center of the device, as shown in the inset of Fig. 3.1, has a small gap ranging from a few to a few 10s of nanometers.

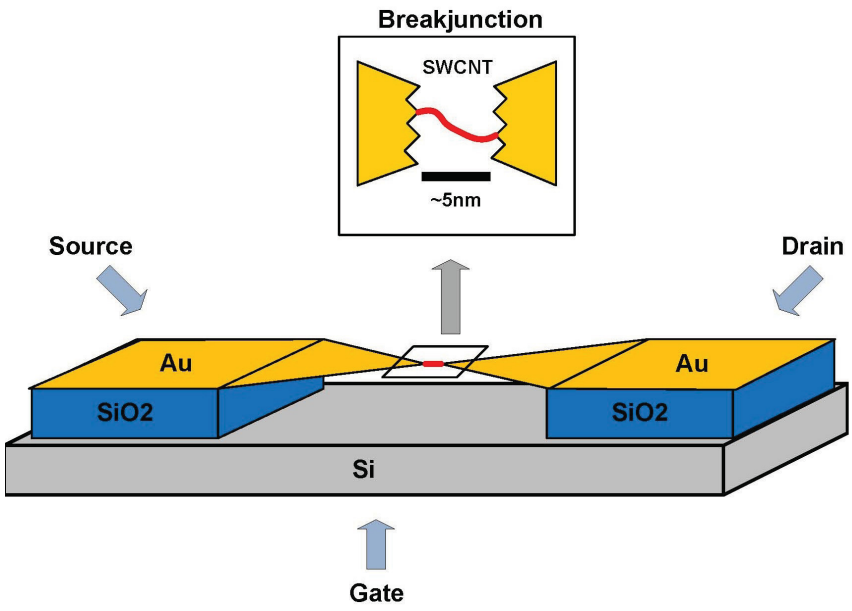

Figure 3.1: Suspended SWCNT device design. The source and drain electrodes connect to the breakjunction which is suspended above the gate electrode. A few-nanometer gap is made in the breakjunction by electromigration.

We now describe each step of the fabrication process of the device shown in Fig. 3.1 except for the final step of electromigration (the process used to make a few nanometer gap in the breakjunction) which is presented in chapter 4.

3.1.1 Reactive Ion Etching (RIE)

We start with heavily-doped four inch silicon wafers with a 300 nm layer of oxide grown on both sides. We etch the backside of these wafers to provide a connection to the backgate which we will later use to tune the carrier density of the nanotube. We etch following the steps described below.

First we use an oxygen plasma etch to clean the chamber and then place the wafer backside up inside the chamber. Once the chamber is pumped down, the power is increased slowly while making sure that the reflected power is less than 15% of the total power. We etch the SiO_2 using a CHF_3/O_2 plasma held at 100 $mTorr$ and 300 W power for 15 min. The CHF_3 is flowed at 22.5 ccm and the oxygen gas at 2.5 $sccm$. Because of the toxicity of CHF_3 we purge the chamber before we open it. We flow nitrogen for 2 seconds and then purge the chamber three times in a row to ensure the CHF_3 is gone. We do a final oxygen plasma etch to clean the chamber.

3.1.2 Photolithography

In the first step of photolithography, we use the patterned mask in Fig. 3.2a. to define catalyst pads. These catalyst pads are necessary to seed the nanotube growth. The procedure is as follows.

We first dice the wafer, with its backside etched, into three pieces to fit our mask. These are cleaned in acetone and rinsed with isopropanol (IPA). Each piece is then spun at 4000 rpm for 30 seconds with Shipley 1813 positive photoresist to provide

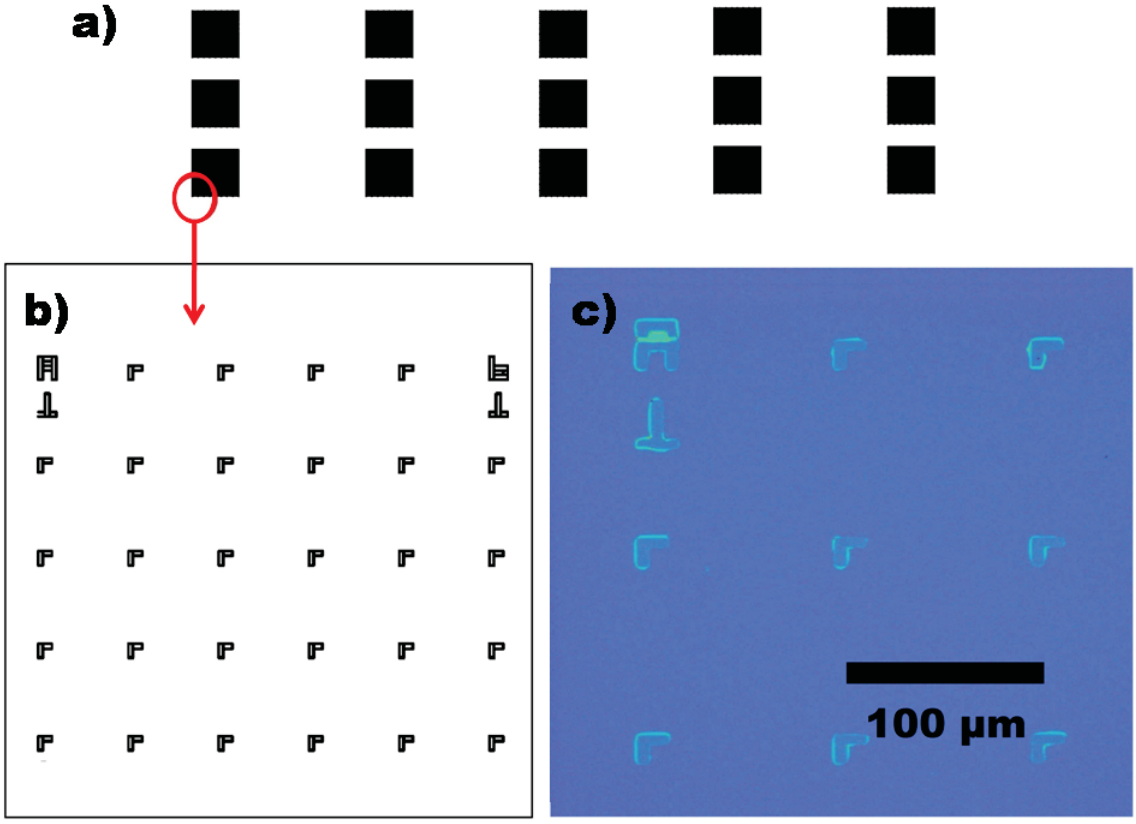

Figure 3.2: **a.** Photolithography mask pattern, 5 sets of 3 grids for 15 grids total. **b.** A complete grid contains letters from A to I and numbers from 1 to 9. **c.** Iron deposition. The submonolayer ($\approx$ 6 $\mathring{A}$) of iron is barely visible under an optical microscope.

a resist thickness of $\sim 1.4\ \mu m$. We soft bake the resist for 1 minute at 115 °C to evaporate extra solvent in the resist making it more susceptible to UV light. We then expose it with the mask at a dose of 35 mJ/cm^2 in hard contact mode. Finally, the piece is developed in MF-319 for 45 seconds and rinsed thoroughly in water. The portions of the resist which were exposed to UV light have a decreased chemical resistance to the developer and are etched away while the non-exposed regions remain. After drying the water, we check the development under a microscope and follow the same procedure for the last two pieces, adjusting the exposure or development time slightly depending on the result.

3.1.3 Sputtering - Iron Catalyst

Sputtering is one of the easiest ways to deposit the iron needed to create the catalyst pads for CNT growth. We sputter a submonolayer of iron, see Fig. 3.2b., ≈ 6 $\mathring{A}$ thick[1]. The iron forms nanoparticles when annealed at high temperature. The diameter of the resulting tubes is directly related to the size of the nanoparticles [29]. Therefore, the amount of iron catalyst is important to ensure that we only grow single-wall tubes. We sputter the iron catalyst according to the following steps.

The photolithographically defined polymer grid is placed in an evacuated chamber and turned away from the iron target. An argon plasma is created using a RF matching unit. The plasma ignites around 30 W and 10 $mTorr$ pressure. The power

[1]Problems with liftoff at first gave us a false sense of the amount of deposited iron. We started with only ≈ 2 $\mathring{A}$ which resulted in high growth yield. Later we found that due to poor liftoff, the iron film had actually folded over onto itself. Once the poor liftoff was resolved the yield substantially decreased and we found that ≈ 6 $\mathring{A}$ is needed to find tubes at nearly every catalyst site.

is increased to 150W while keeping the reflected power below 5 W. The deposition rate was previously determined through a long deposition to be ≈ 2.5 $\mathring{A}/min$. The substrate is turned toward the target and deposition begins. After a 6 $\mathring{A}$ deposition the substrate is moved away from the target and the power is slowly decreased and the substrate is removed.

The substrate is then placed in acetone to remove the iron from the unexposed portions of the resist from the photolithography step. Since it is a submonolayer it lifts off quickly in hot acetone (60 °C).

3.1.4 Chemical Vapor Deposition (CVD) - Growth

The growth of nanotubes is still somewhat of an art and the exact growth dynamics are unknown. In our lab we use a recipe that combines results obtained from a few different groups [30, 31, 32]. Our growth is done in a Thermo Scientific furnace. We built a custom gas mixing panel, see Fig. 3.3a., with two digital flow controllers to precisely control the hydrogen and methane flows in addition to a rotameter to control the argon flow. Check valves were installed after each flow controller to ensure single directional flow. The one inch diameter quartz growth tube is connected at each end with a pair of vacuum actuated leak proof seals. The leak proof seals are essential to avoid air leaks in our low flow growths. Just before the growth furnace we installed a flash arrestor to quickly suppress any potential fire in the gas line. This home-built system works very well and yields excellent tubes. The growth details are described according to the steps below.

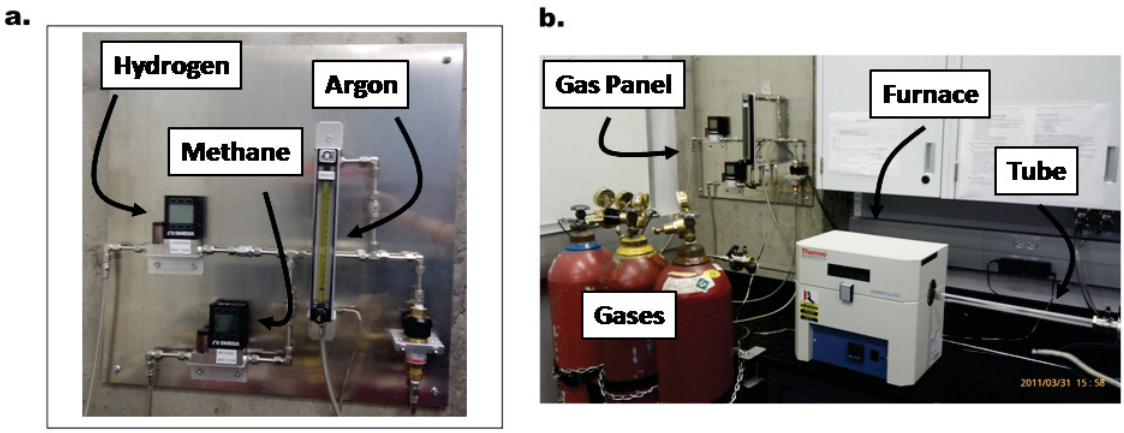

Figure 3.3: **a.** Gas mixing panel. Three gases are mixed controllably using two digital flow meters and one rotameter. After being mixed, the gases flow through a fire arrestor in case of line fire. **b.** Thermo Scientific furnace and growth tube connected with gas lines. The gases flow from the tanks to the mixing panel, through the furnace and out to a fume hood. (This system was built by J. Island with supervision by A. Champagne.)

We have found that comparably low flow rates ($\approx$ 0.2 standard liters per minute (SLM)) are sufficient for growth on our substrates (SiO_2 on Si) with an iron catalyst and our recipe very much resembles that of Ref. [33]. We start by cleaning the substrate with acetone and then rinsing with IPA. The substrate is placed at the center of the furnace inside a 1 inch diameter tube. The substrate is cut slightly smaller than the tube is wide to make sure it sits in the center of the tube. The furnace is heated to 900 °C in atmosphere to anneal and form the iron nanoparticles. After 1.5 hours the furnace is cooled back down to about 400 °C at which point the gas lines are connected to the tube as in Fig. 3.3b.. An argon flow of 0.1 SLM is started and the furnace is heated back up to 900 °C. At 900 °C, a flow of hydrogen at 0.1 SLM is introduced and the argon flow is stopped. For 20 mins the hydrogen

treats the iron nanoparticles and leads to better wetting [34]. The furnace is raised to the growth temperature of 970 °C. After three minutes to stabilize the temperature, the growth gas, CH_4, is flowed at 0.2 SLM and allowed to flow for 45 mins. After growth, the CH_4 is turned off, argon is turned back on at 0.1 SLM and the hydrogen is also turned off. The furnace is allowed to cool down to 400 °C at which point we open the furnace to speed up cooling. At 200 °C the argon is shut off and the plumbing is disconnected to remove the chip.

3.1.5 Photolithography - Alignment Marks

We now repeat the photolithographic procedure described above but with the purpose of creating gold alignment marks that we will later use to align breakjunctions on the nanotubes (see Fig. 3.4). The details are described below.

We use the same mask as earlier and align the chip with grown nanotubes underneath so that the original catalyst grid is slightly offset from the soon to be exposed grid. This way, we will have nanotubes between the grids used for alignment. It is essential that these grids be exposed with sharp edges to allow high-resolution e-beam lithography alignment. We evaporate 5 nm Ti, for adhesion, and 80 nm of gold. We then liftoff in hot acetone and check the quality of the lithography.

3.1.6 Finding Tubes - Scanning Electron Microscope (SEM)

With the alignment marks in place, we now use an SEM to find tubes and take images that will be used to locate the tubes within the grids. An example is shown in Fig.

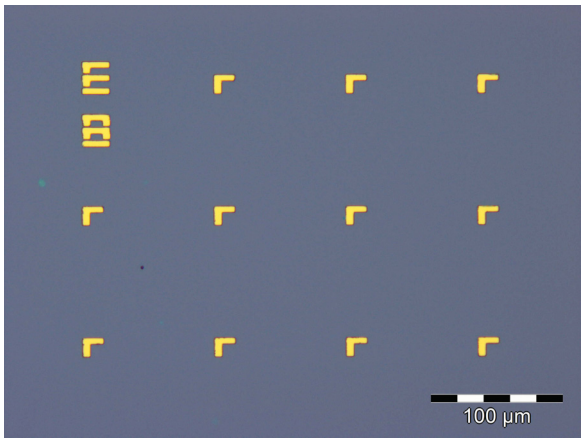

Figure 3.4: Gold alignment marks after the second step of photolithography. The Fe pads and nanotubes on the chip are not visible under optical microscope.

3.5. With the correct amount of catalyst we get tubes within nearly every set of four L-shapes. A low accelerating voltage (2 kV) is used to produce the most scattering events. This makes the nanotubes easy to see and deposits less contamination but at a loss of resolution. We look for tubes that are long so that we can place three breakjunctions on one tube within a single four corner grid. This gives us more opportunity for alignment of a breakjunction on top of a tube.

3.1.7 Imaging Tubes - Atomic Force Microscope (AFM)

Now that the location of the tubes is known, we use AFM for high-resolution imaging of the tube's diameter. It is difficult to determine whether our tubes are single or double walled based on diameter alone. In Ref. [35] they find a large overlap for single and double wall tube diameters. In chapter two we mentioned that the smallest diameter single-wall tube has a of diameter of $0.41nm$, from Ref. [12], and in Ref.

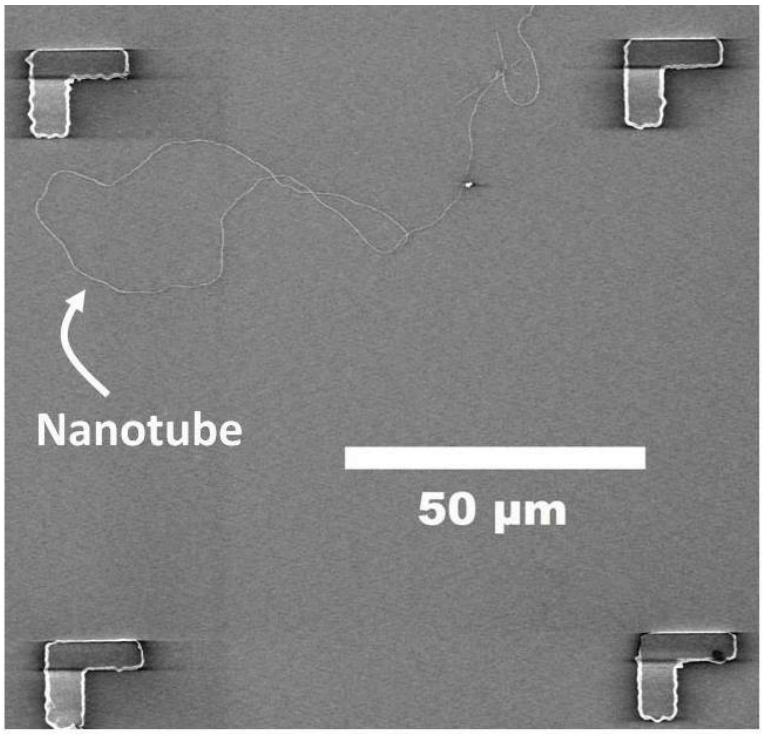

Figure 3.5: An SEM image including the alignment marks to later locate the nanotube within the L-shapes. The nanotube diameter is larger in appearance due to the low magnification and low accelerating voltage.

[35] they measure double wall tube diameters down to 1.8 nm. This gives us a range for single-wall tubes but electron transport will be used for the final determination of which type we have. Multi-wall tubes have much higher overall conductance than single-wall tubes. The tube diameter will be used in calculations for mobility and mean free path later. We take an average over more than 200 scans of the tube height, as in Fig. 3.6a., to determine the tube diameter. In the case of Fig. 3.6b. we measure a height of 1.1 ± 0.4 nm. We use an average of 1.1 nm for our calculations in chapter 5 which is from a sampling of three tubes.

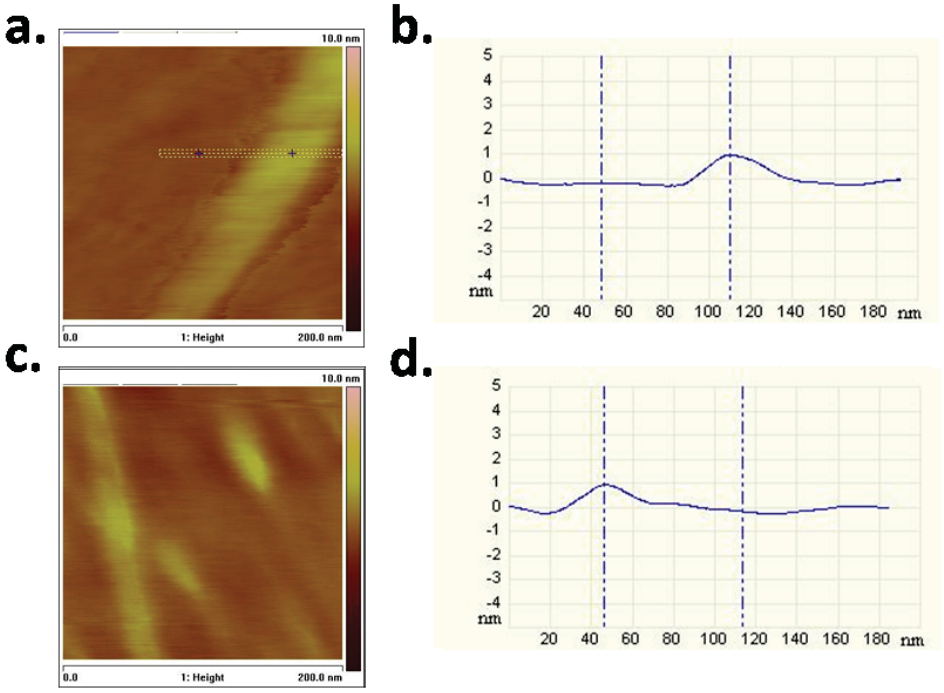

Figure 3.6: **a.** A 200 nm AFM scan of a nanotube. We take the height measurement by averaging more than 200 section cuts across the tube. **b.** The average of the difference between the tube height and surface height. Here the diameter of the tube is 1.1 ± 0.4 nm. **c.** Another tube from the same growth. **d.** The measurement height is 1.1 ± 0.5 nm

3.1.8 Making Contacts - Electron Beam Lithography (EBL)

In this step we lay down gold breakjunctions on top of the nanotubes. The precision of the alignment of the breakjunctions is limited in several ways. The SEM image, taken at 700× magnification to include the 100 μm spaced L-shapes, has a limited resolution and therefore a nanotube diameter of only a few nanometers appears on the image to be a few hundred nanometers. This is also due to the low accelerating voltage used. The Nano Pattern Generation System (NPGS) software we use for EBL has an alignment accuracy of about 200 nm. We make the junctions as wide as possible ($\sim 320nm$) to handle these limitations but only to the point where it is still possible to later electromigrate the junctions reliably.

We start the EBL process by drawing a grid of 2x2 μm squares on the SEM image, as in Fig. 3.7a., to locate the tube within the alignment marks. We use this grid to create a Computer-Aided Design (CAD) file which defines the breakjunction on top of the nanotube. An alignment file is created that has the same shapes and dimensions as the alignment marks on our chips. We then spin the chips with copolymer and PMMA. This bilayer process gives us good liftoff after deposition of gold. First we spin the copolymer at 4000 rpm for 1 min and bake the chip for 15 mins at 170 °C. After cooling for a minute we spin the PMMA at 2000 rpm for 1 min and bake again at 170 °C for 15 mins.

With the EBL we locate the position of the nanotube and run the alignment file to precisely expose the breakjunction pattern on top of the nanotube, as in Fig. 3.7b..

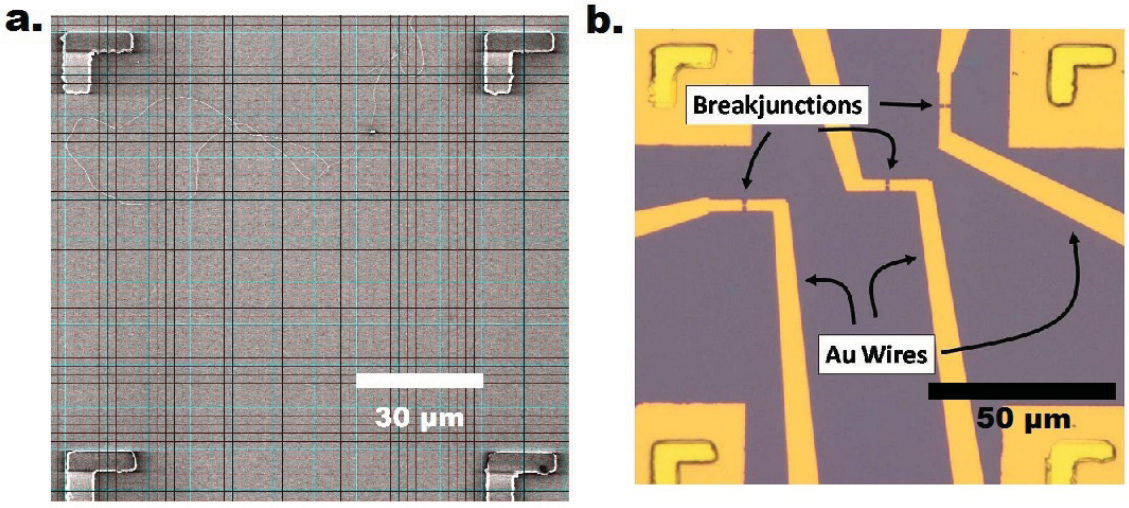

Figure 3.7: **a.** A 2x2 μm grid is drawn on top of the SEM image to locate the nanotube. **b.** Three Au breakjunctions are placed on the nanotube at different locations. The Au squares around the L-shapes are from the alignment step of the e-beam exposure.

This is where the precision of the second photolithographic step matters. L-shapes with sharp edges provide accurate alignment of the breakjunctions. Adjusting of the contrast during the alignment helps discern small details for accurate alignment. After the exposure of the breakjunction pattern, we develop the chip in MIBK:IPA (ratio 1:3) for 30 secs, methanol for 15 secs, and finally rinse in IPA for 15 secs. To facilitate electromigration we only evaporate 40 nm of gold, without an adhesion layer, for the breakjunctions and then liftoff in hot acetone. In Fig. 3.8, individual SEM images of three breakjunctions (after EBL) have been superimposed on top of a larger image of a nanotube. The breakjunction images are slightly transparent to see the tube run through the junction. It shows the precision of our alignment.

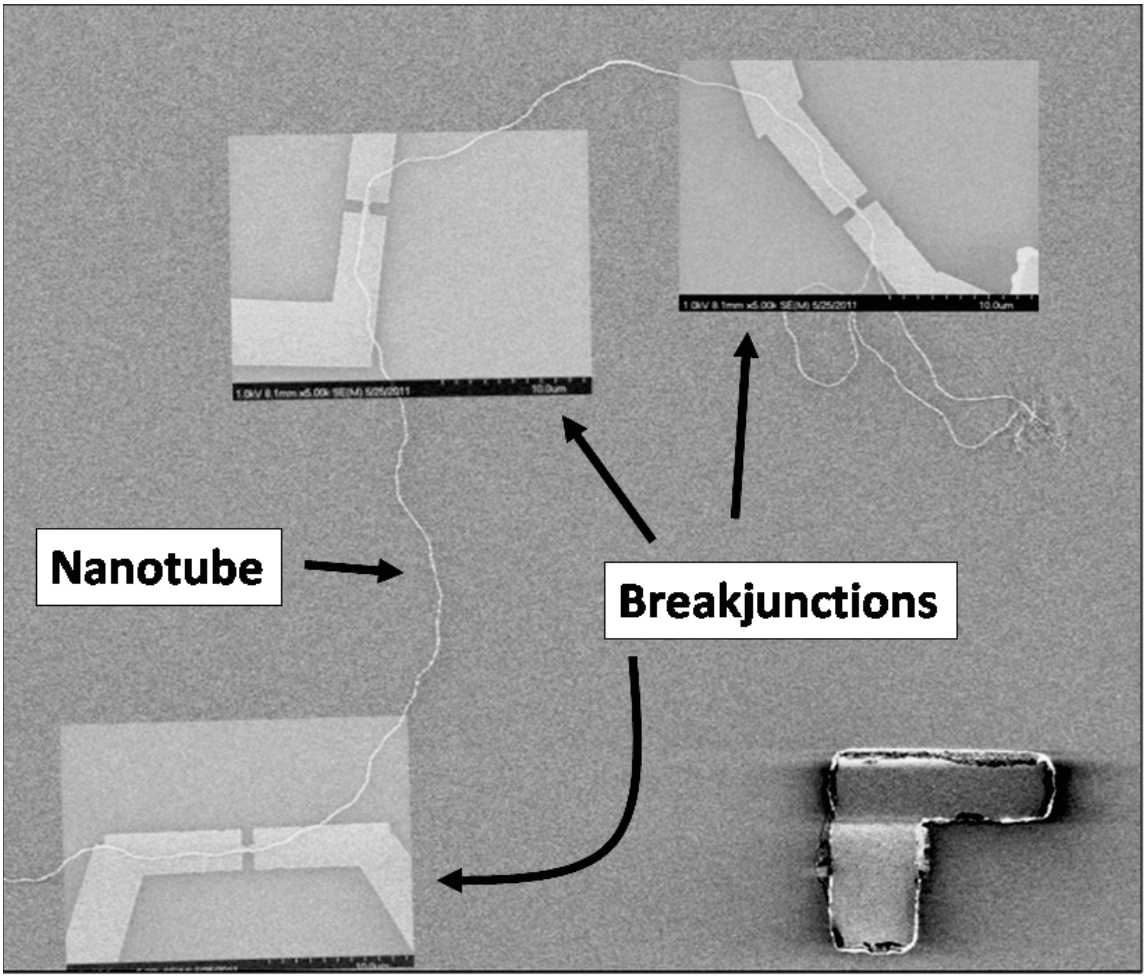

Figure 3.8: Three breakjunction SEM images superimposed on top of a larger SEM of the nanotube. The breakjunction images are slightly transparent to see the tube run through the junciton.

3.1.9 Contact Pads - Photolithography

The 40 nm of gold film evaporated for the breakjunctions is not thick enough to wire bond (micro-weld a wire to the gold), so we add another step of photolithography to define larger contact pads and evaporate a thicker layer of gold, see Fig. 3.9. The process is slightly different at this step because now the chips have been diced into individual grids. Each grid contains about six breakjunctions depending on the nanotube yield.

Chips with single grids are spun with S1813 and baked as in the previous photolithography steps. We use a mask that has several patterns so the chip must be aligned to the position of the 6-pad pattern on the mask, 2 pads for each junction. Once attached, we wax the chip to a wafer and load it into the system along with the exposure mask. The chip is not necessarily flat so we must expose the chip in proximity mode which allows us to adjust the distance of the mask above the chip. The mask, made of Fe_2O_3, is semi-transparent which allows us to align the large contact pads with the smaller contacts connected to the breakjunctions. Once the contacts are aligned, we move the optical camera to the corner of the chip and raise the chip toward the mask until Newton rings appear. When we have Newton rings on three corners of the chip we know that the chips is flat relative to the mask and ready for exposure. We expose at 40 mJ/cm^2. After exposure the chip is developed for 45 secs in MF319 and checked under a microscope. We then evaporate a 5 nm adhesion layer of Ti and an 80 nm layer of Au with a subsequent liftoff.

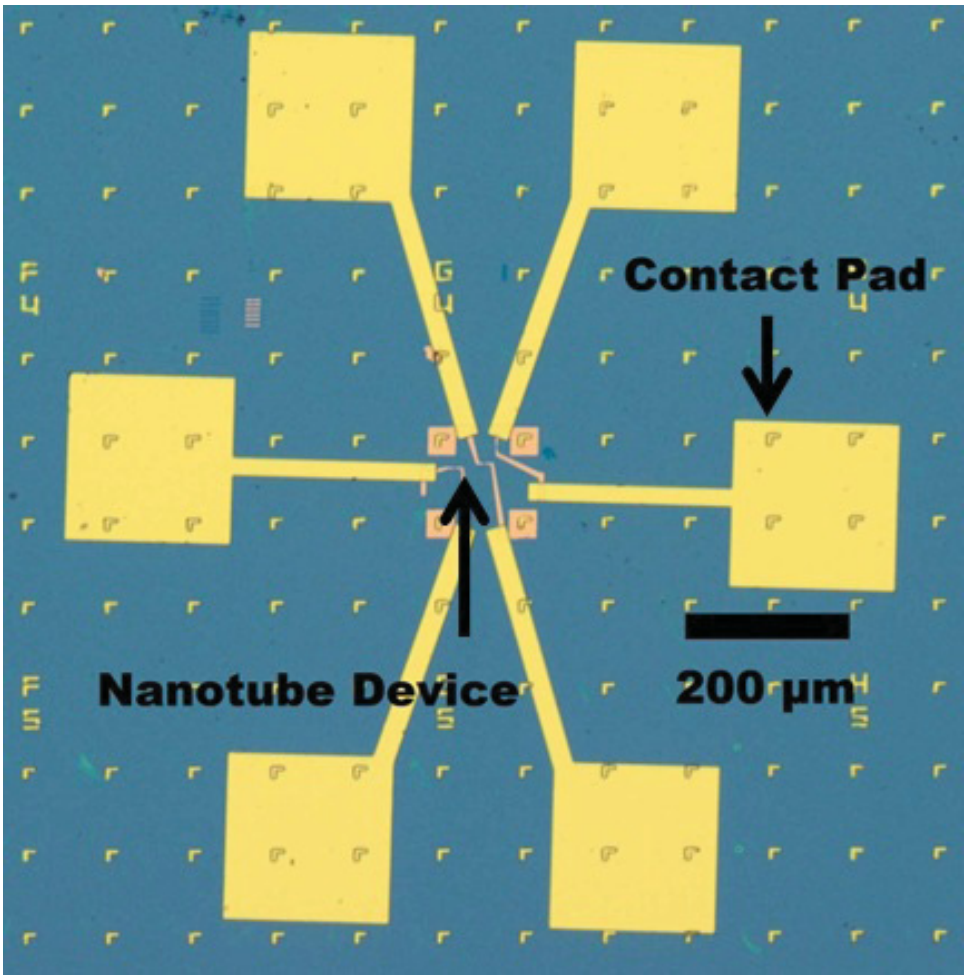

Figure 3.9: Large contact pads are defined to connect to the breakjunctions created by e-beam lithography.

3.1.10 Suspension - Hydrofluoric (HF) Acid Etch

The next step is to suspend the breakjunctions as seen in Fig. 3.10. This is done by etching away the SiO_2 underneath the junctions. We suspend the junctions enough so that the bow-ties at the center of the junctions are suspended completely but the bars connecting the bow-tie are still held up by oxide. The suspended junctions allow for mechanical stretching of the device, facilitate in the electromigration process, and remove substrate disorder to make ultra-clean SWCNTs.

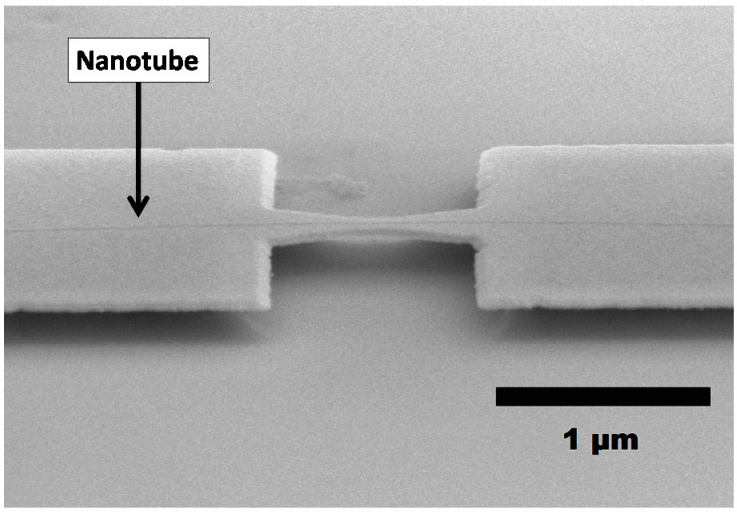

Figure 3.10: Suspended breakjunction after HF etch. The nanotube runs underneath the junction. In this case the nanotube diameter is large enough to see the tube underneath the gold.

First, the etch rate of the buffered HF solution is calibrated by etching a blank chip from the same wafer as the chips with the junctions. The blank chip is etched for 1 min then thoroughly rinsed in at least 6 subsequent beakers of water. We use an

ellipsometer to measure the thickness of the remaining oxide and calibrate the etch rate according to this. Once the etch rate is known we etch the samples in the same way except that after the rinse in water the chip is transferred to another beaker with IPA. The IPA has a lower surface tension than water and when dried in a nitrogen stream the junctions will remain suspended. We take the first chip and check it with SEM, as in Fig. 3.10, to make sure the junctions are suspended correctly and then etch the rest.

3.1.11 Wire Bonding

These suspended junctions with large contacts are then wire bonded (see Fig. 3.11). We connect the back of the chip, with the exposed silicon, to a chip carrier with silver paint. Wires are attached to the large pads, first from the grounded carrier and then to the pads connecting the junctions, and double bonded for added security. The gate is connected by bonding a wire to the floor of the chip carrier which is connected to the silicon substrate.

3.2 Data Acquisition

Data acquisition is done using custom made software and instrumentation. We insert the chip carrier into a socket that is mounted on the end of a top loading probe as shown in Fig. 3.12**a.** which is inserted into a cryostat, Fig. 3.12**b.**.

The Cryostat is capable of making measurements from 1.5 K to 420 K in vacuum

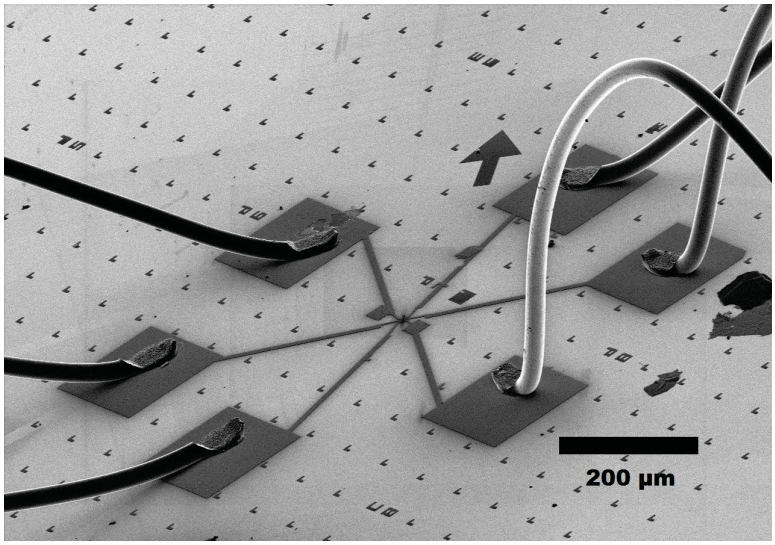

Figure 3.11: The chip is fixed to a chip carrier and then wire bonded to allow connections to the breakjunctions. Image courtesy of Vahid Tayari

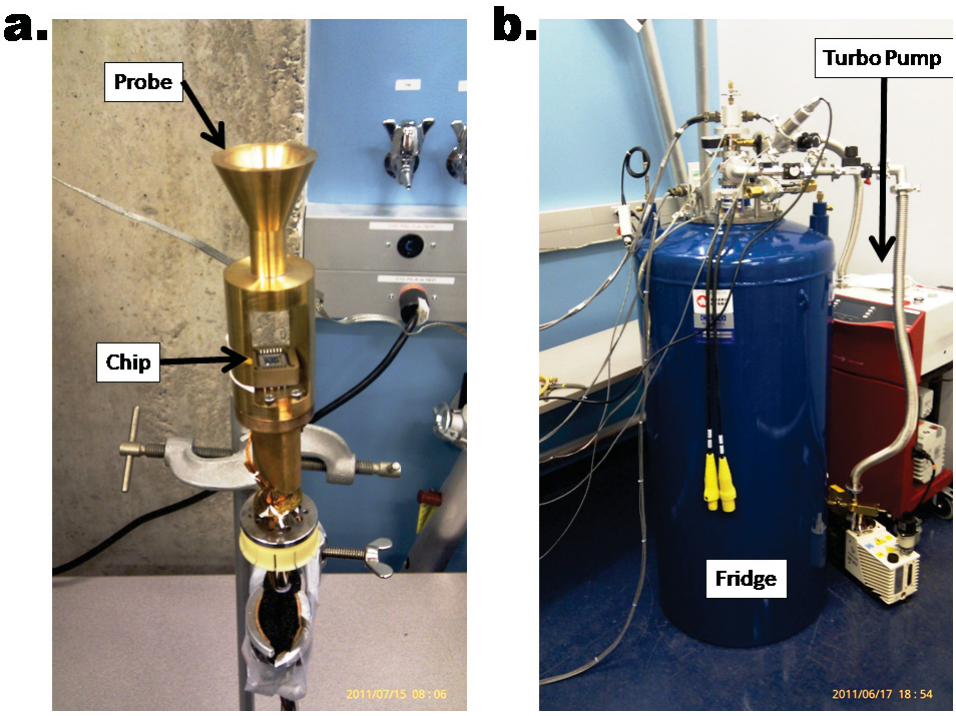

Figure 3.12: **a.** Top loading probe with device mounted on the end. **b.** Helium-4 fridge with turbo pump. The probe is loaded into the fridge to make measurements.

provided by a turbo pump. The turbo pump can reach a pressure of 1×10^{-7} *torr*. The circuit shown in Fig. 3.13 is set up using a BNC breakout box connected to a data acquisition card. The data acquisition card, installed in the CPU, provides the bias voltage and receives the drain current from the current preamplifier. The gate voltage is supplied from a Keithley voltage source that runs through a filter before going to the sample.

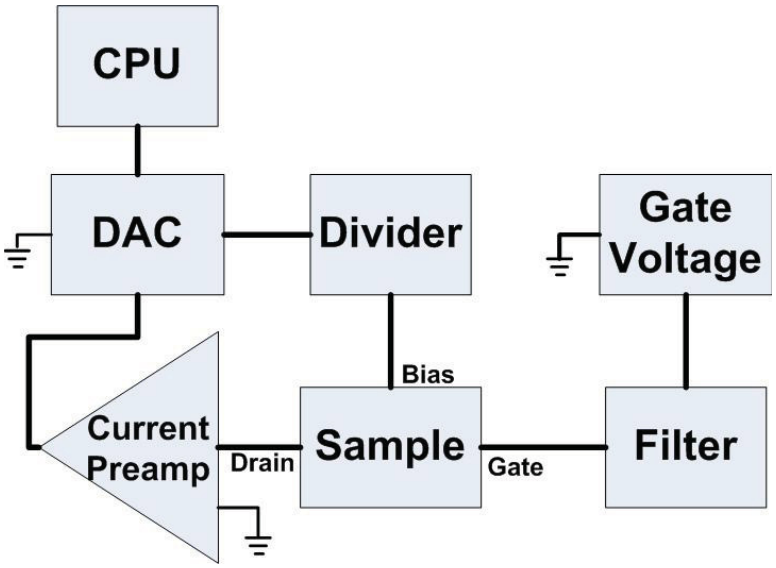

Figure 3.13: Measurement circuit set-up. The CPU controls the DAC which supplies the bias voltage and receives the drain current. The gate voltage is supplied form a Keithley DC voltage source.

3.2.1 Software

We coded software that is capable of making 1D sweeps (IV curves), 2D sweeps (I vs. V_b, V_g), and 3D sweeps (I vs. V_b, V_g, and T). The graphical user interface is shown in Fig. 3.14. The current, bias voltage, gate voltage, and temperature are all shown

in real time during any of the three types of sweeps. Once a sweep is completed the data is saved to a text file for import into the Igor analysis software.

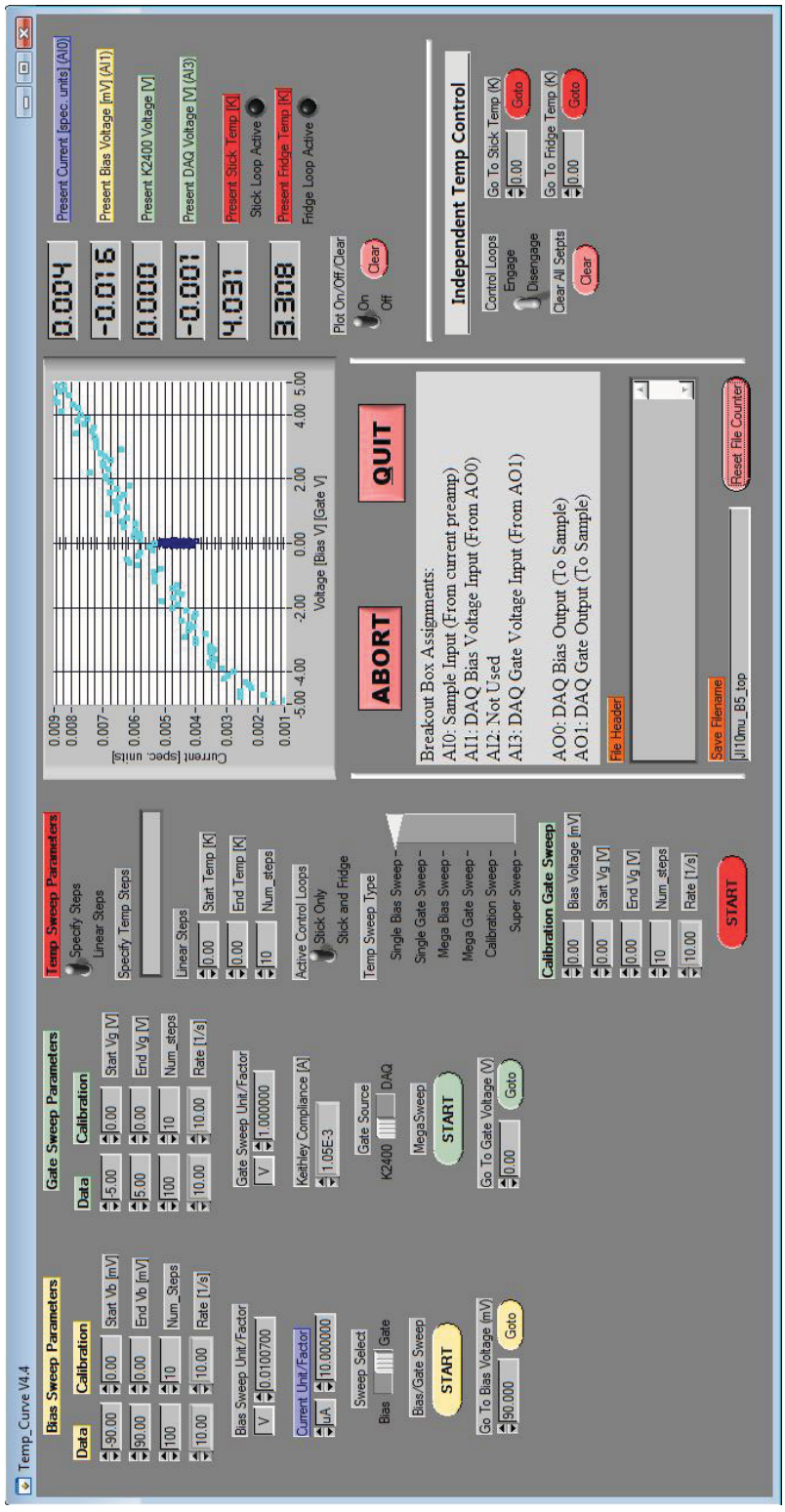

Figure 3.14: Temperature Curve V4.4, data acquisition software capable of multidimensional automated sweeps. (Coded by J. Island)

Chapter 4

Controlled Nanometer Gap Creation

We are now ready to create few-nm carbon nanotube NEMS. In this chapter we describe the method we developed to create few-nm gaps in the suspended gold junctions fabricated in chapter 3. Electromigration is a well known phenomenon in nanoelectronics. At high biases, high energy electrons collide with the atoms of a conductor and diffuse them. Several groups have used this technique to create nanometer spaced electrodes [36, 37, 38, 39]. Exciting applications of these nanometer spaced electrodes have been realized by taking the electromigrated junctions and studying single molecules by depositing the molecule between them [40, 41, 42, 43]. We present, for the first time, the creation of nanometer gaps in suspended breakjunctions on carbon nanotubes. We further developed the electromigration technique to create gaps of varying sizes by breaking the junction at different selected

powers.

We start by reviewing the software that we coded based on a feedback system to controllably create few-nm gaps in the gold breakjunctions. With the knowledge of how the software runs, an explanation of the full electromigration process follows. We then describe the process we recently developed to create gaps of varying sizes by breaking the junction at precise powers. Finally, we describe the high current annealing process used to clean the devices after breaking.

4.1 Electromigration Software

The electromigration software is capable of functioning in two different modes, automatic and manual. See Fig. 4.1 for an image of the graphical user interface (GUI). In manual mode, the rate and size of the applied voltage steps is set. The voltage ramps up according to these parameters and the software plots the results in real time. Upon some change in the resistance of the junction, as seen by a change in the slope of the plot, the sweep can be paused or reversed to arrest the breaking of the junction. In this way, the gold can be etched away after several iterations of sweeping forward and back. We found that the manual mode alone is insufficient for breaking the junctions. In the automatic mode, the starting voltage, forward rate, reverse rate, and reverse step size are chosen, as well as a reverse trigger percentage and maximum resistance. The trigger percentage is the percentage of the initial resistance at which the program will start decreasing the voltage to arrest breaking. Typically, this

percentage is 1%-3% at the beginning and reaches 20% for higher resistances. When a trigger event occurs in the automatic mode, the software will reverse the voltage to the junction according to the set parameters. Once the backward sweep is complete, a new initial resistance is set and the voltage is increased according to the forward step parameters. The maximum resistance is the resistance at which the program will stop the electromigration process and quickly ramp the voltage to zero. Multiple runs of the software are required because as the resistance of the junction increases the gain on current preamplifier must also be increased which in turn affects the sensitivity of the trigger percentage. Typically, the initial maximum resistance is set at 500 Ω and is increased in steps. The real-time resistance, voltage, current, and trigger percentage are all displayed in the GUI during the sweep. The data is saved to a text file after the complete sweep ends.

4.2 Controlled Nanometer Gap Creation By Electromigration

In Fig. 4.2 we plot the current vs. voltage for the first step of the electromigration of a device. We will use this as a guide to explain the process.

First, the bias voltage to the junction is slowly increased at 5 mV/sec. As the voltage is ramped up the junction heats up causing the resistance to increase slightly. At $\approx 0.6V$, the electrons flowing through the junction have enough energy to knock the gold atoms out of the narrow part of the junction. The resistance of the junction

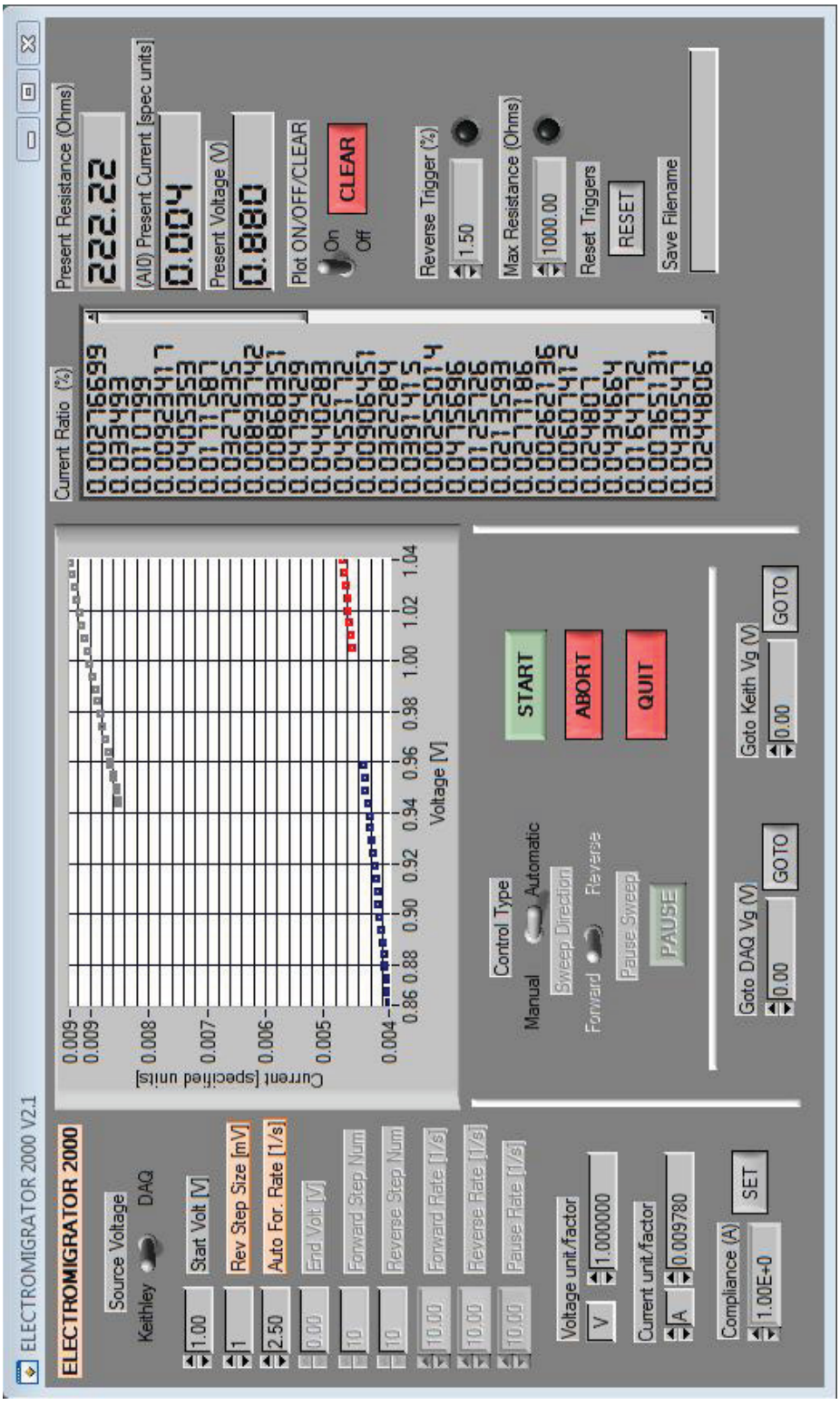

Figure 4.1: The Electromigrator 2000, electromigration software. Automatic and manual modes are available to create a small gap in breakjunctions. (Coded by J. Island)

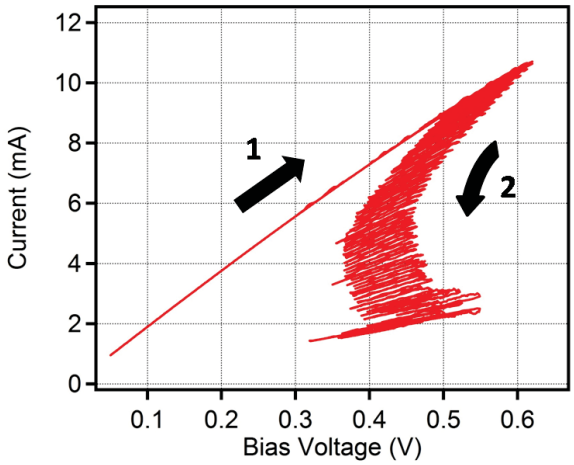

Figure 4.2: Electromigration data plot. The software steadily increases the voltage across the junction until the resistance changes at which point the software decreases the voltage quickly to stop the breaking of the junction.

slowly increases as more and more gold is etched away. Each time the resistance increases to this breaking point, the software ramps down the voltage quickly to prevent complete explosion of the device. Without this ramp down an avalanche breaking of the junction will occur and the junction will explode, destroying the device and creating a micron size gap in the junction like the one shown in Fig. 4.3.

The software continues etching in this way, ramping up and down the voltage to gradually increase the resistance of the junction to 500 Ω at which point the program ramps the voltage back to zero. The sample is grounded and the gain on the drain and the reverse trigger are increased to compensate for the increase in noise for highly resistive devices and the software is started again. The software again etches the gold away to a higher resistance (i.e. narrower gold wire) and the gain and trigger are adjusted. After each step, an IV curve and gate sweep are taken to check the

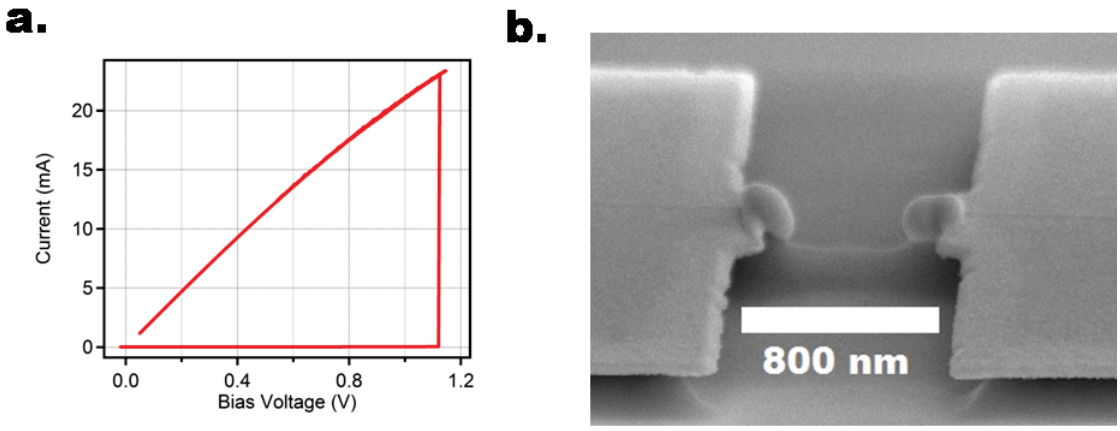

Figure 4.3: **a.** Data plot for a junction where the voltage was not ramped down soon enough. **b.** SEM of the junction after avalanche explosion.

response of the junction. Once the gold has been etched away enough to leave a gap bridged only by a nanotube the resistance of the device will be greater than 7000 Ω corresponding to the minimum resistance for a SWCNT.

4.3 Gap Creation By Selective Breaking

The full process described above will create a gap of minimum size (a few nanometers). We further developed the process to create gaps of different sizes by breaking the breakjunction at precise power values. The process starts in the same way but the first electromigration step is not fully completed. In the first step, we etch the gold junction to a desired resistance. The sweep in Fig. 4.4**a.** is an example of this first step where the gold junction has been etched to a resistance of 38.9 Ω.

The process is stopped and started once more. The voltage to the junction is increased

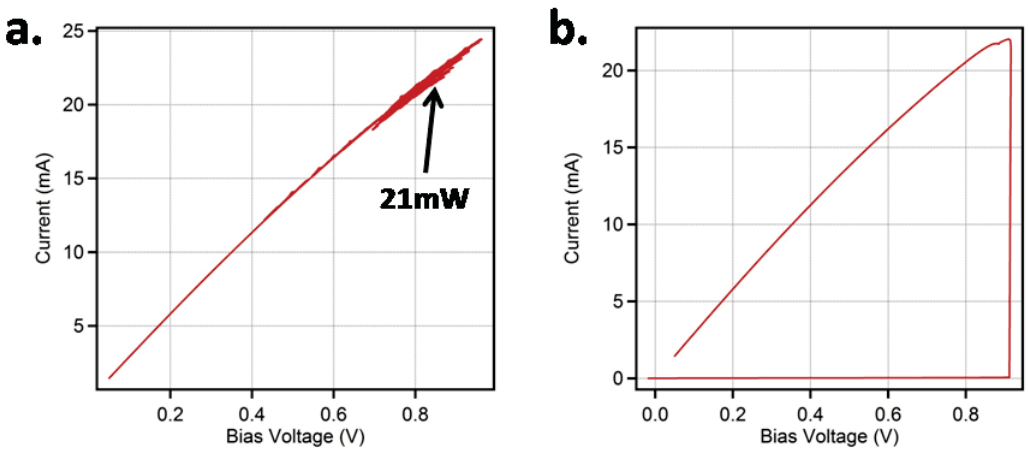

Figure 4.4: **a.** First step of the controlled gap creation by one-shot break etches the junction to the desired resistance. **b.** The second step breaks the junction at the desired power and quickly ramps down the voltage to save the tube. The SEM for this junction is shown in Fig. 4.5

until the it breaks completely at the power of the first step $P = V_{Bias}/R$, as seen in Fig. 4.4**b.**, and then it is ramped down quickly to save the tube. In Fig. 4.5 we show the gap created by the above process. A gap of $\approx 70\ nm$ was created at a breaking power of 21 mW.

By adjusting the first step we can control the power at which the junction breaks and therefore the size of the final junction. To illustrate this, in Fig. 4.6 we display a review for several junctions broken at various powers. With increasing power there is an apparent increase in the gap size. Although it is not completely linear, gaps of $\approx 10\ nm$ are created at lower powers ($< 20\ mW$) and gaps of $\geq 20\ nm$ at higher powers ($> 20\ mW$). The technique is being developed to improve the yield and better control the gap sizes.

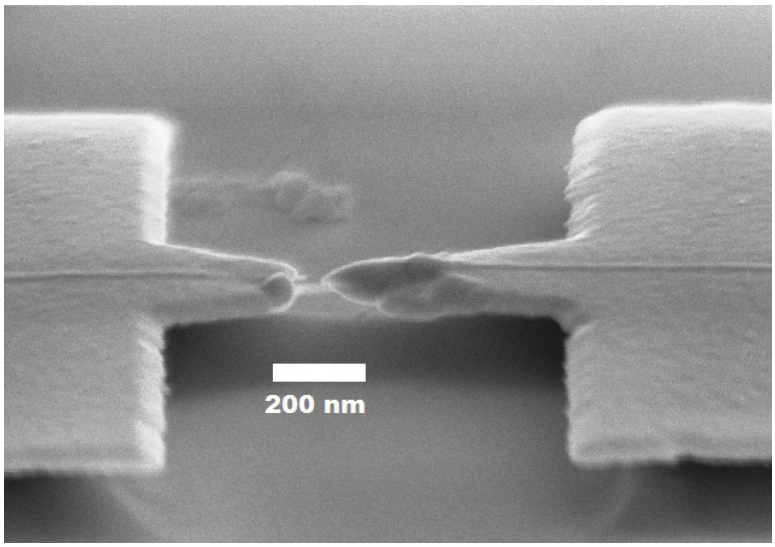

Figure 4.5: SEM image of gap formed in a breakjunction by electromigration. The gap is $\approx 70\ nm$. The gap was created by breaking the junction at 20 mW power.

In terms of software parameters the first step of the controlled gap creation is identical to the full electromigration process. In the second step however, the trigger is set to maximum so that the voltage is never ramped down until the junction has been broken. The maximum resistance is set to a few thousand ohms to ensure that when the junction breaks the voltage will be ramped down as quickly as possible to save the tube.

4.4 Annealing

As a result of the fabrication process, the nanotubes will have impurities (resist, water, and gold) on them which affect their electrical and mechanical properties. To clean the devices we send a high current through them which heats them up and

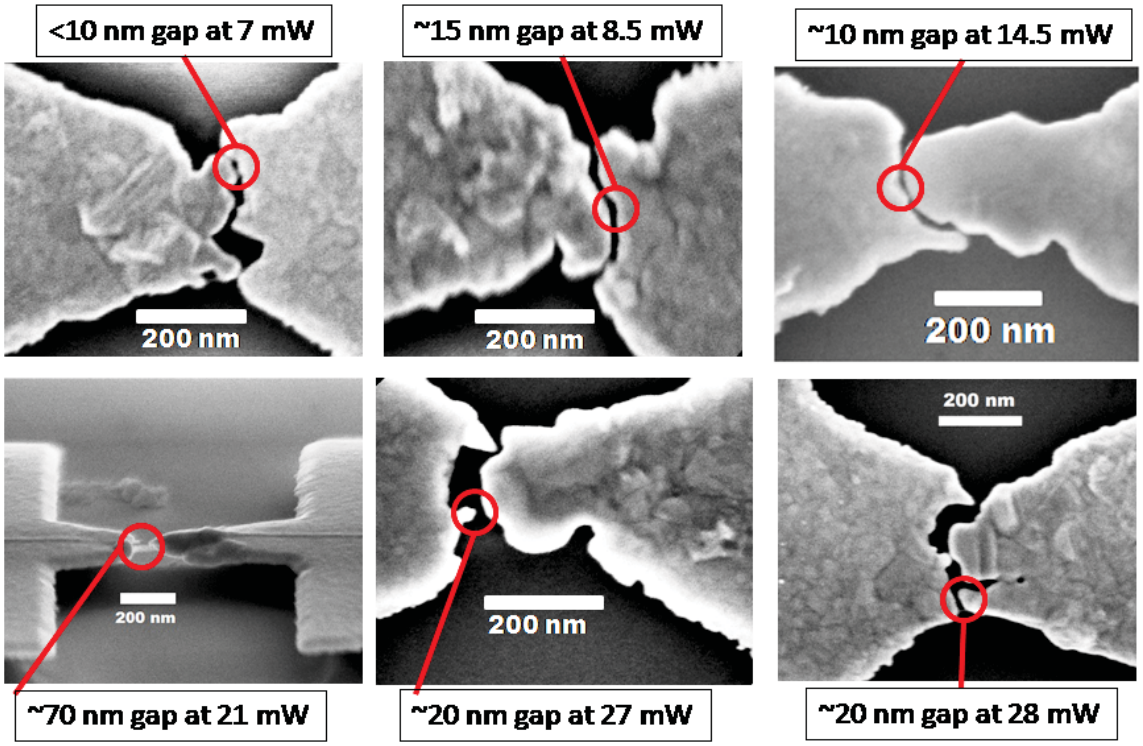

Figure 4.6: Gap creation review. SEM images for six breakjunctions that were broke at increasing powers. While the gap size does not scale exactly linearly with the power there is a grouping of two categories. In the top three SEMs gaps of approximately 10 nm are created for powers less than 20 mW and in the bottom three SEMs larger gaps $\geq$ 20 nm are created at higher powers.

ashes away the unwanted impurities. Typically, the currents used are a few μA but can reach tens of μA depending on the device. We use the electromigration software in manual mode to slowly increase the voltage across the device until reaching the desired current, then pause the ramp to keep a constant voltage applied to the device as shown in Fig. 4.7 where we plot the I-V data for the annealing process of one device. After 10 mins at constant bias, the voltage is slowly ramped back down.

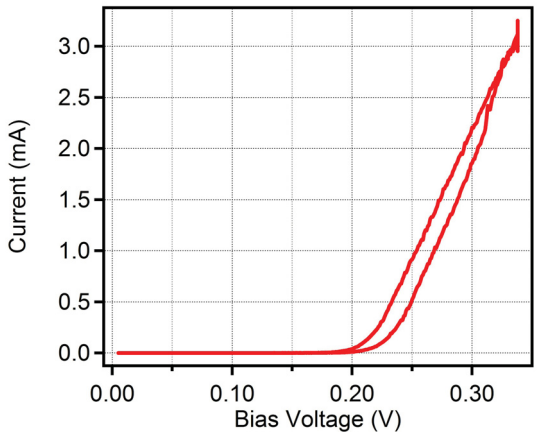

Figure 4.7: High current annealing. We ramp up the voltage slowly using the manual mode of the electromigration software and then pause at the desired current. We then wait 10 mins to clean the device and finally ramp down the voltage.

In Fig. 4.8 we plot the conductance for a device that has been annealed once at 3 μA (1 μW) and then again at 5 μA (2 μW). A clear increase in conductance is seen in the gate sweep corresponding to a cleaner device after each anneal.

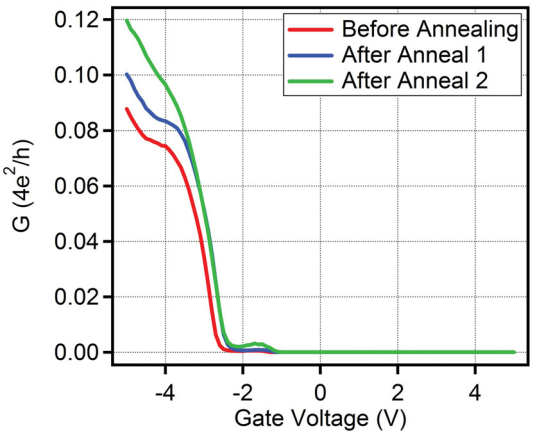

Figure 4.8: High current annealing results. The conductance of the device increases with each high current annealing step. The first anneal was done at 3 μA (1 μW) and the second was done at 5 μA (2 μW)

4.5 Graphene NEMS transistors

The power of the gap creation method is that it is not restricted to nanotube devices. In our lab we also use this method to create graphene NEMS transistor. The fabrication is done much in the same way as here but instead of a nanotube there is a single layer of graphene underneath the breakjunction. In Fig. 4.9 we have a small gap created by electromigration in a breakjunction with graphene instead of a nanotube. The software in automatic mode responds in the same way with a nanotube or graphene and opens the door to NEMS creation of other novel materials.

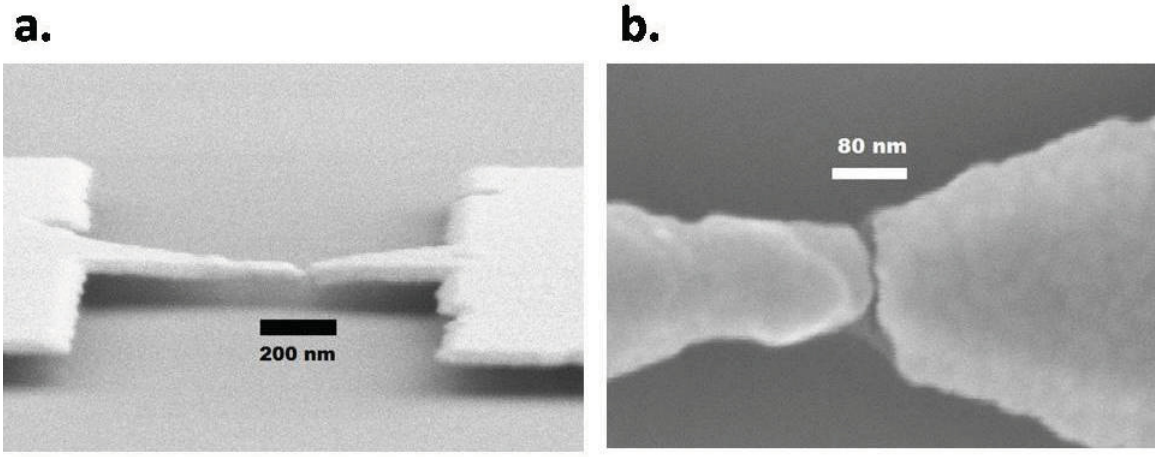

Figure 4.9: SEM image of a gap formed in a breakjunction with graphene instead of a nanotube. **a.** Tilted image of the junction. **b.** Top view image. The width of the gap is $\approx 140nm$ and the length is $5 - 10nm$. Images courtesy of Vahid Tayari.

Chapter 5

Electronic Spectroscopy of Suspended Few-nm CNT

In electronic spectroscopy, tunneling electrons are used to probe the band structure and excitations of crystals. Here, we inject electrons into few-nm CNT devices and measure conductivity as a function of the carrier density (V_{gate}) and energy of incident electrons (V_{bias}). The use of electronic spectroscopy to probe our ultra-short devices is extremely useful since their vibrational excitations are up to the terahertz range which is out of the range of high-frequency electronic measurements.

We measure both the stretching and flexural (bending) modes in these devices. In devices displaying stretching mode vibrations we measure vibrational frequencies up to $9\,THz$. We extract a coupling factor of $g = 2.2$ which is among the largest ever seen in suspended nanotube devices [6, 7]. Larger coupling factors have been measured but are attributed to the special device geometry used to make the measurement

[7]. Here, the coupling measured is a property of the entire device. In a device displaying flexural mode vibrations we measure vibrational frequencies exceeding 600 GHz. Traditionally, a radio-frequency antenna or the mixing of two AC signals is used to drive the resonance frequency of the bending mode which is then measured through transport [3, 26, 28]. Here, we measure the bending mode through tunneling electrons which can reach much higher frequencies.

In the first section of this chapter, we use the equations from chapter 2 to extract the properties of an on-substrate CNT quantum dot using data from a 2D ($I-V_{bias}-V_{gate}$) plot. The last sections presents the data from three NEMS quantum dot devices, fabricated following the procedure presented in chapter 3 and 4, which display vibronic excitations. We calculate their electron-vibron coupling constant (g) from the Frank-Condon model and extract the frequency and quality factor for these NEMS devices.

5.1 Electronic Excited States

In chapter two we discussed the theory of a SET and reviewed how to extract the device properties from the Coulomb blockade data. Before we present the data for our suspended few-nm devices, we first look at a quantum dot device on substrate and study its electronic excitations. In Fig. 5.1 the white diamonds mark the locations of charge ground states where there is a Coulomb Blockade.

The height of diamond #1 is the charging energy plus the single particle level spacing, $E_C + \delta$, and it is taller than the three successive diamonds by the electronic level

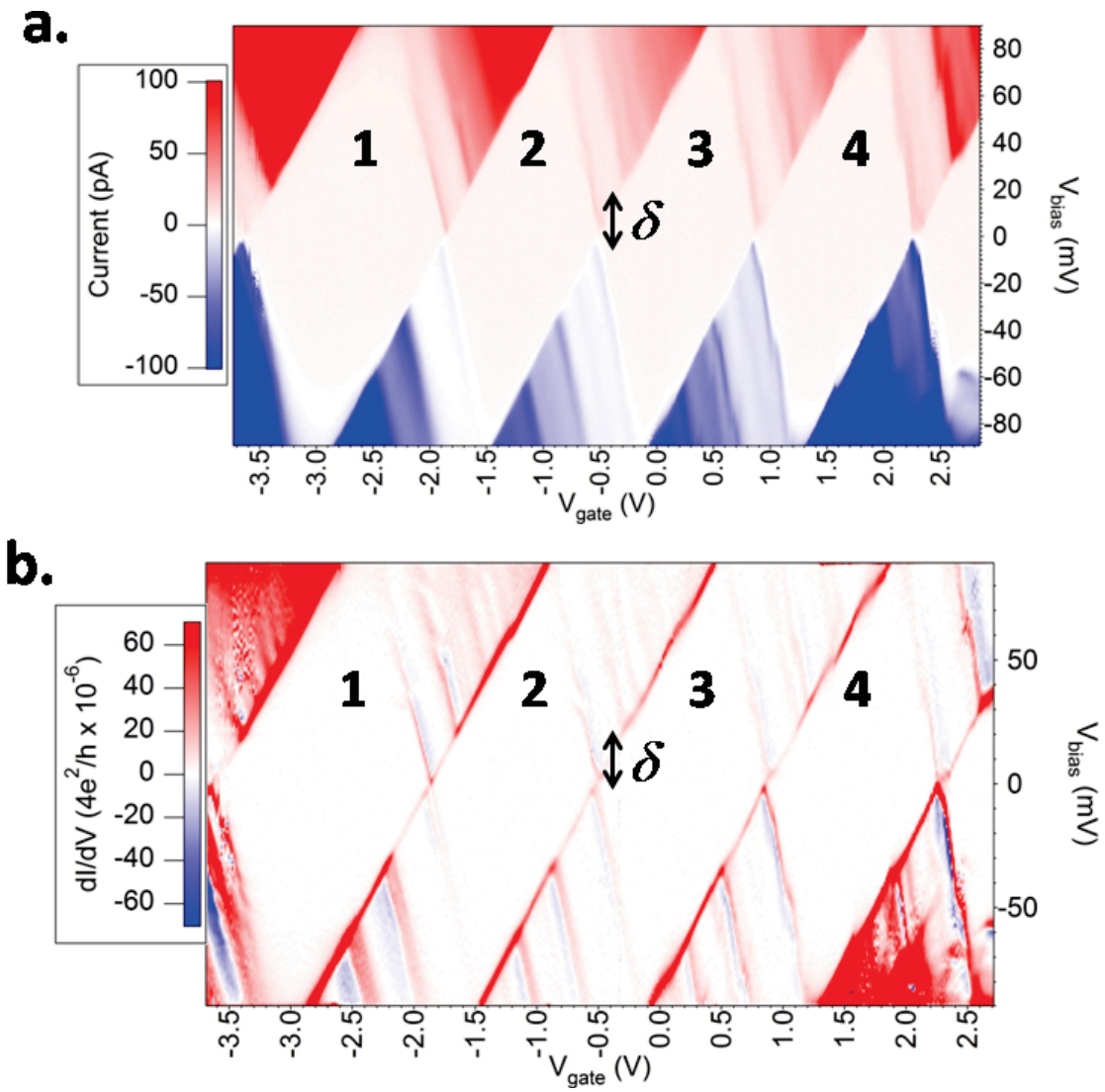

Figure 5.1: 2D Contour plot of the electron transport data for an on-substrate nanotube quantum dot. **a.** Four-fold degeneracy of the nanotube band structure is seen by one larger diamond followed by three smaller ones. **b.** Plotting the differential conductance shows clear lines for excited electronic states. The energy of the excited electronic state is shown and is 20 meV

spacing, δ. The three successive diamonds show the four fold degeneracy of the nanotube energy structure and therefore their height is $E_C + 0$. The appearance of the four fold degeneracy in the data reflects the cleanliness of the crystal.

Following the analysis of chapter 2 we can first extract the capacitances for this device from the 2D plot. The gate capacitance is given by the width of the diamond, $C_G = e/\Delta V_G$ where ΔV_G is the width of the diamond. The gate capacitance for this device is $C_G = 0.09\ aF$. From the relations in Fig. 2.9 we calculate a source capacitance of $C_S = 0.38\ aF$ and a drain capacitance of $C_D = 0.87\ aF$. From the capacitances we calculate the charging energy for this dot, $E = 88\ meV$, which is in agreement with the height of the coulomb diamond as discussed in chapter 2. Finally, we can also extract the electronic excitation energy $\delta = 20\ meV$ from the contour plot in 5.1.

5.2 Few-Nanometer Devices

In Fig. 5.2 we have plotted the current/voltage characteristics for one of our suspended few-nm nanotube devices (device A) measured at 4 K.

A clear current blockade is visible as diamond regions in Fig. 5.2**a.** but there are a number of differences from the 2D plots we saw in chapter 2. Most notably, the current is much stronger for the negative gate (hole doping) transport than for the positive gate transport because the device is a p-type semiconducting nanotube. The depletion of the holes is shown in the left panel of Fig. 5.2**c.**.The leftmost diamond has

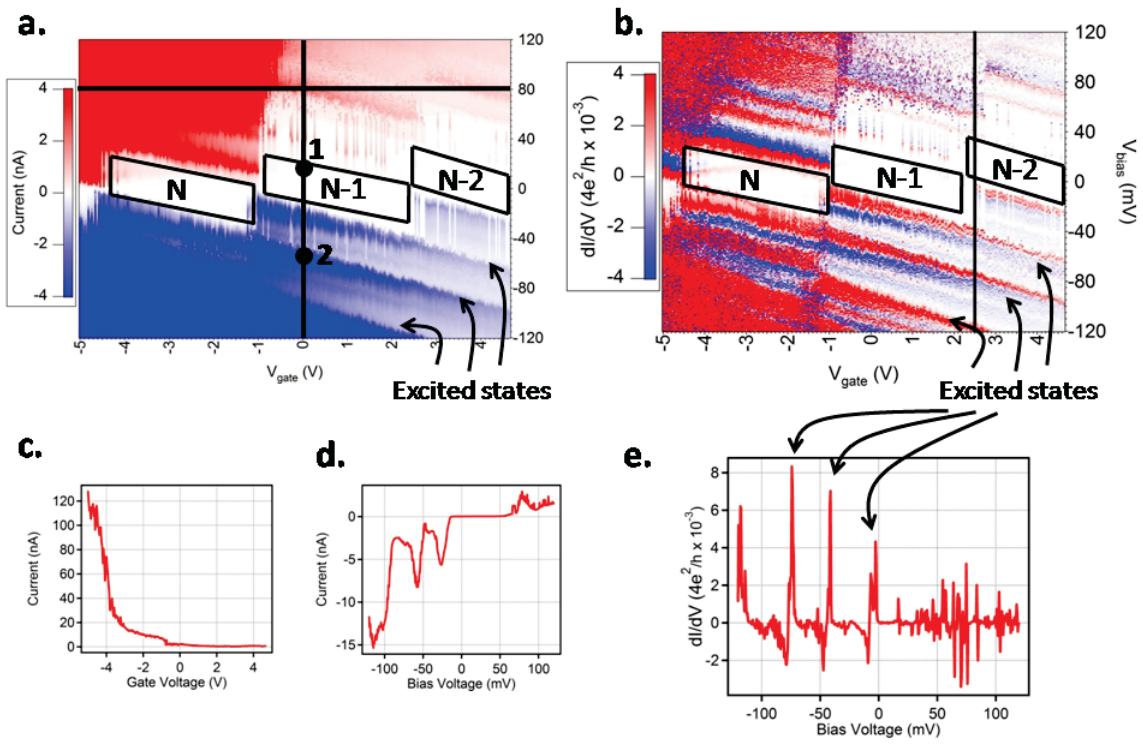

Figure 5.2: **a.** 2D contour plot of the measurement data for device A. The leftmost diamond is a ground state with N holes. The horizontal black line indicates the position of the gate sweep shown in **c.**. The vertical black line indicates the position of the bias sweep shown in **d.**. The numbered positions show the location of a vibronic absorption peak (1) and emission peak (2), see the text for explanation. **b.** The same data but plotted with the differential conductance (dI/dV) on the z-axis. The black line marks the location of the bias sweep shown in **d.**. **c.** shows the gate sweep from **a.** showing the p-type behavior of the semiconducting tube. As the gate voltage changes from left to right, the holes are slowly depleted form the tube. **d.** Bias sweep from **a.** where excited states are seen as steps in the I-V curve. **e.** The bias sweep from **b.** gives peaks for excited states.

N holes (labeled in Fig. 5.2**a.** for clarity) and for each successive diamond there is one less hole on the dot. The diamonds are skewed which is a result of the asymmetrical tunnel barriers to the nanotube dot.

We again extract the capacitances from the Coulomb diamonds in Fig. 5.2**a.**. From the gate capacitances we can calculate the length of the tube using Eq. 2.12[1]. We summarize these values in Table 5.1 along with the values for two other devices[2].

Table 5.1: Parameters for three nanotube devices

	$C_G\ (aF)$	$C_D\ (aF)$	$C_S\ (aF)$	$E_C\ (meV)$	$L\ (nm)$
Device A	0.04	0.12	4.76	32.5	5.0
Device B	0.03	0.39	4.32	33.8	3.8
Device C	0.32	0.92	1.80	52.6	24.7

5.3 Stretching Mode Vibrons

In Fig. 5.2**b.** we plot the differential current as a function of the bias and gate voltages for device A. The lines of positive differential conductance (the peaks in Fig. 5.2**e.**) correspond to excited states of the nanotube quantum dot. The energies for these excitations, following from chapter 2, are measured as the energy positions of the peaks. The energies are averaged over the entire plot for each peak to give an excitation energy of $38 \pm 4\ meV$ for device A. Data on device B reveals an energy of

[1]Although our devices are only 5 nm long the gate voltage is applied to the entire tube running under the gold contacts so the model of a wire above a wall is still appropriate.

[2]SEM images of devices A and B after measurement verified a length of $< 10\ nm$. We estimate a suspension of 10 nm for device C and the SEM image verifies a gap of 20 nm.

$\approx 35\ meV$. The excitations for device C are discussed in the next section.

We argue that these excitations are not electronic in nature but in fact correspond to quanta of mechanical vibrations called vibrons. The first evidence for this is the energy of electronic excitations for our devices. Devices with a tube length of 5 nm have electronic excitations, from Fig. 2.14, of 335 meV. The excitation energies for samples A and B are nearly ten times less than this electronic excitation energy. Using Eq. 2.20 we can extract the length of the stretching mode vibrons in the system from the excitation energy. For device A we calculate a length of $L_V = 1.3\ nm$ and device B a length of $L_V = 1.4\ nm$. The vibron lengths are about three times less then the device lengths calculated from the Coulomb diamonds in Table 5.1. This is consistent with observations in other suspended nanotube devices [7]. It has been shown that a device with a vibron smaller than the dot size has local varying Franck-Condon factors which is an explanation for the negative differential conductance (NDC) (strong blue peaks in 5.2) that is found alongside the excitation peaks [24].

The second evidence for vibronic excitations is the appearance of a vibronic absorption peak located within the Coulomb diamond at position 1 in Fig. 5.2**a.**, at high temperature [7]. As the temperature of the system increases so does the vibronic population. The absorption of a vibron can help electrons tunnel across the dot giving a "vibron assisted" current in the regions of blockade. At the same time, as temperature is increased the peak corresponding to tunneling of electrons which emit a vibron on the dot weakens (located at position 2 in Fig. 5.2**b.**). As k_BT gets

larger it broadens the excited level and decreases dI/dV. We plot the temperature dependence of position 1 (absorption) and 2 (emission) of Fig. 5.2**a.** in Fig. 5.3.

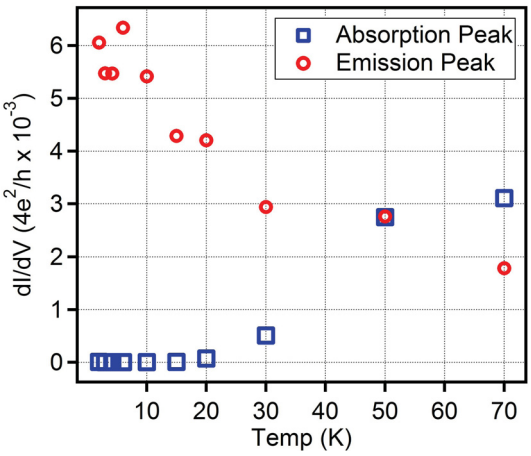

Figure 5.3: Temperature dependence of the emission and absorption peak shown in Fig. 5.2.

The final evidence for vibronic excitations is a suppression of current at low biases called Franck-Condon blockade as discussed in chapter 2. In 5.2**d.** the current around zero bias is suppressed compared to the larger biases. This blockade is a result of the coupling between the tunneling electrons and the vibrons. There are four peaks in the negative 1D bias sweep which correspond to the ground state (peak near 0 V) and three excited vibronic states. By fitting the Franck-Condon progression, Eq. 2.19, to the peaks in 5.4 we can extract the coupling constant for this device. The fit gives a coupling factor of $g = 2.2 \pm 0.4$.

By comparison, Sapmaz et al. [6] found a coupling factor of unity for a suspended nanotube of 420 nm.

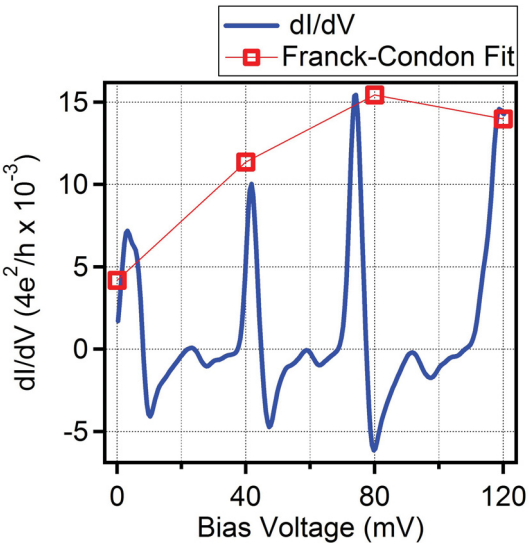

Figure 5.4: Fit of the Franck-Condon progression, Eq. 2.19, for the four states in Fig. 5.2**d.**. The fit gives $g = 2.2 \pm 0.4$.

5.4 Bending Mode Vibrons

In chapter 2 we briefly mentioned that the bending mode couples to electrons quite differently than the stretching mode reviewed above. In Fig. 5.5 we plot (dI/dV 2D) data for device C. The SEM for this device is in the bottom fright panel of Fig. 4.6 and the gap is $\approx 20\ nm$.

In Fig. 5.5**a.** we show the 2D plot for the device before annealing. A few excitation peaks are present but they are not periodic and the Coulomb diamonds are deformed. We clean the device by high current annealing (see chapter 5) to ash away the impurities on the nanotube that affect its mechanical and electronic properties. The anneal was done at a current of 4 μA (1.3 μW) for ten minutes.

The first recognizable difference after the anneal (Fig 5.5**b.**) is the overall increase in

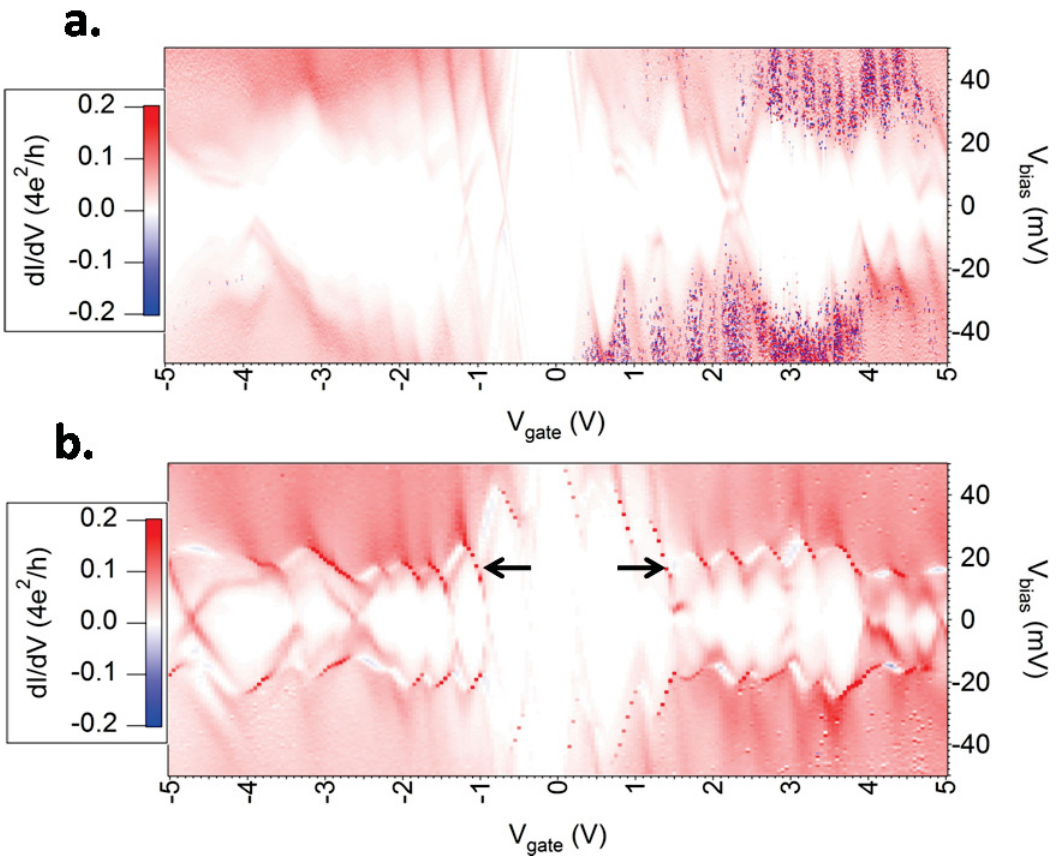

Figure 5.5: **a.** 2D data plot for device C before high current annealing **b.** 2D data plot for device C after annealing. Strong dI/dV peaks follow the tops of the coulomb diamonds and represent driving of the out-of-plane bending mode.

conductance for the device. More importantly though, there is a high conductance resonance line that follows the tops and bottoms of the Coulomb diamonds. This resonance corresponds to the excitation of the bending mode vibron. The bending mode couples to electrons through strong positive feedback as explained in chapter 2 [26, 27]. This mode appears in devices with a high quality factor, Q, because when an electron tunnels at a rate greater than the resonance frequency for the mode it can excite on resonance the bending mode vibration. With a high quality factor the vibration has a long lifetime and the next tunneling electron is more likely to couple to the mode again. Electrons trigger the onset of this mode at a specific rate instead of at a specific energy because even though V_{bias} must be larger than $\hbar\omega_{bend}$ to excite the mode, we only observe the mode when the coupling factor (g_{bend}) is sufficiently large. So in order to see these excitations we must clean the device to achieve a high quality factor.

As a first order approximation of the frequency of this mode, we measure the current at the peaks indicated by the arrows in Fig. 5.5**b.**. The current at these peaks gives a tunneling rate of $\Gamma = I/e = 625\ GHz$, where e is the electron charge and $I \approx 100\ nA$ is the current. The energy for this excitation is then $E = hf = 2.6\ meV$.

Upon closer inspection of the conductance regions near the Coulomb diamonds in Fig. 5.6, an excitation peak is found running parallel to the current thresholds. This excitation corresponds to the stretching mode vibron which we saw in device A. The energy for this excitation is $E = 10\ meV$ and gives a stretching mode vibron length

of $L_V = 5\ nm$ using Eq. 2.20. Here, we find the vibron length is again less than the size of the dot as discussed for device A. So, in the same device we see the driving of the bending mode which is found by a strong resonance peak along the top of the Coulomb diamonds and the stretching mode by a excited state in the single electron transistor region.

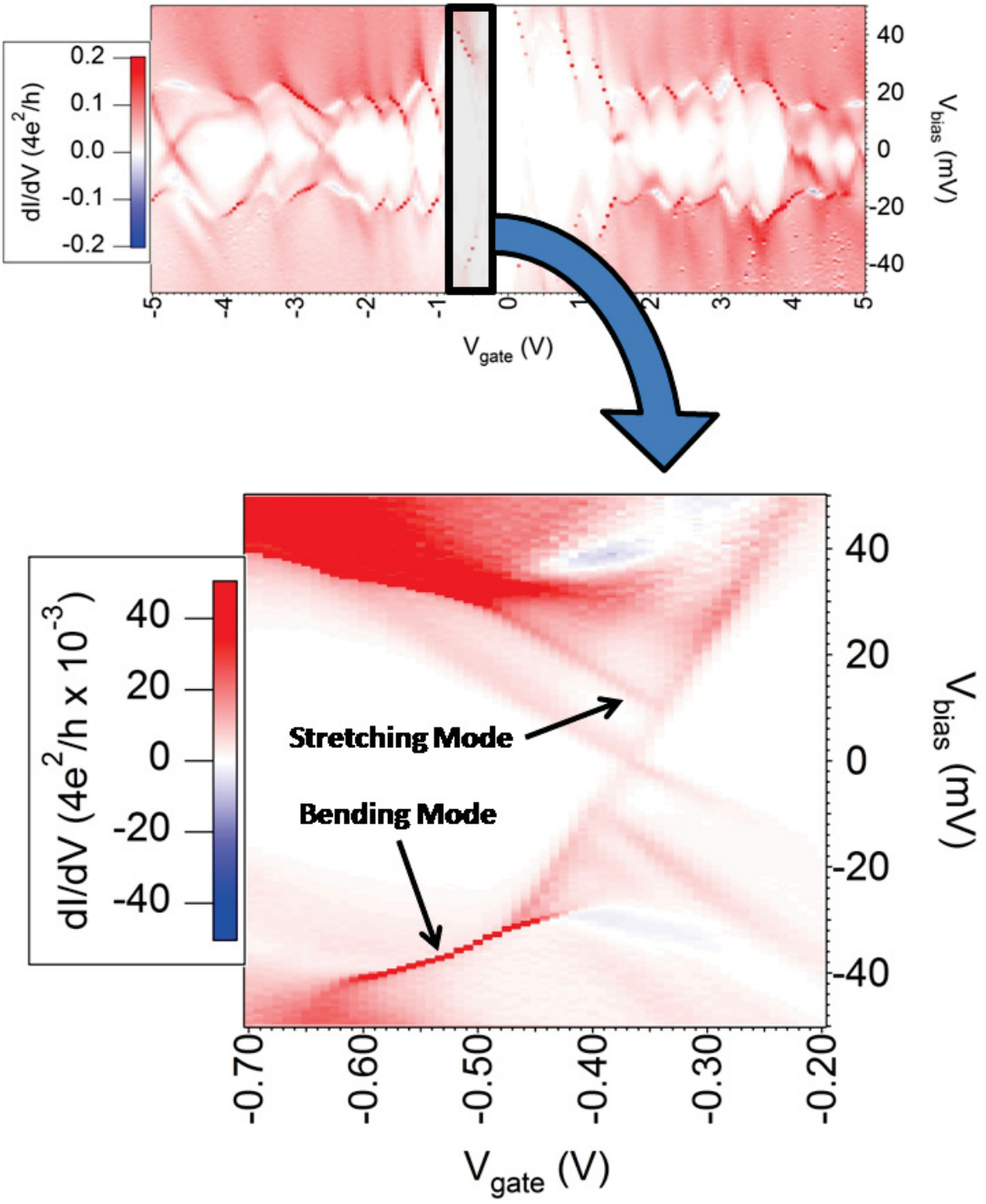

Figure 5.6: 2D plot of the data in Fig. 5.5**b.** around a single conductance cone. The bending mode appears as a sharp resonance line along the top and bottom of the diamond and the stretching mode is an excited state in the SET region.

Chapter 6

Conclusion

We fabricated few-nanometer sized suspended electro-mechanical nanotube transistors and studied the coupling between their quantum electronics and mechanics. We developed a nano-etching technique to controllably create nanometer sized gaps ($3.8 - 70\ nm$) in suspended gold wires (breakjunctions) on top of carbon nanotubes. We measured electron transport at low temperature in these devices.

We observe strong coupling between the tunneling electrons and two different vibrational modes of carbon nanotubes. In ultra-clean carbon nanotube devices we observe a strong driving of the bending mode from charge transport with frequencies exceeding 600 GHz. In other devices we also measure a suppression in low-bias conductivity due to a strong coupling between electrons and the longitudinal stretching mode (Franck-Condon Effect). We extract a coupling factor of ($g = 2.2 \pm 0.4$), among the largest seen in suspended nanotube devices. We measure vibrational modes up to 9 THz in these NEMS.

These devices are an order of magnitude smaller than previously studied devices and offer a rich playground for studying the fundamental physics of quantum electronics and mechanics. We see electrons couple to two vibrational modes in a single device from the data in Fig. 6.1. Future directions for this work include mapping out the coupling factor versus strain (mechanical breakjunction) and length (using the electromigration technique to fabricate devices of various length). We aim to explore the bending mode which could lead to tunable ultra-sensitive THz resonators.

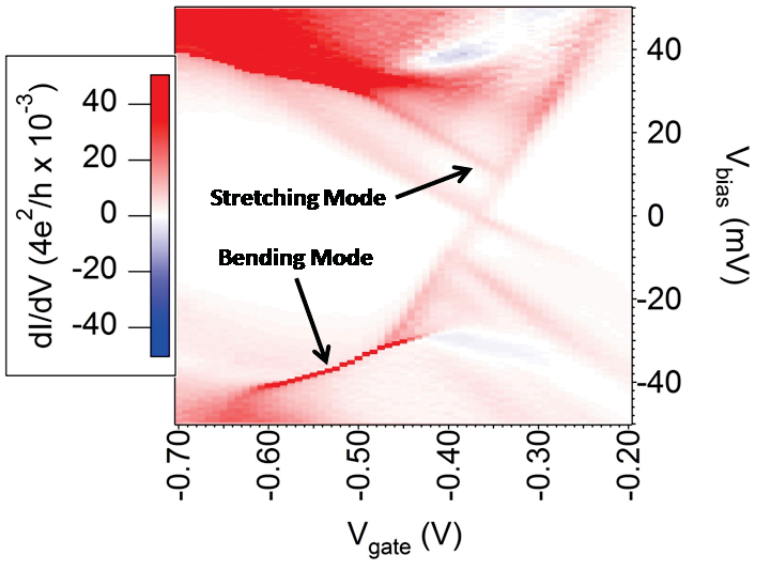

Figure 6.1: 2D plot of the data in Fig. 5.5**b.** around a single conductance cone. The bending mode appears as a sharp resonance line along the top and bottom of the diamond and the stretching mode is an excited state in the SET region.

Bibliography

[1] Hsin-Ying Chiu, Peter Hung, Henk W. Ch Postma, and Marc Bockrath. Atomic-scale mass sensing using carbon nanotube resonators. *Nano Letters*, 8(12):4342–4346, 2008.

[2] K. L. Ekinci, X. M. H. Huang, and M. L. Roukes. *Ultrasensitive nanoelectromechanical mass detection*, volume 84. AIP, 2004.

[3] Vera Sazonova, Yuval Yaish, Hande Ustunel, David Roundy, Tomas A. Arias, and Paul L. McEuen. A tunable carbon nanotube electromechanical oscillator. *Nature*, 431(7006):284–287, 2004.

[4] M. J. Biercuk, S. Ilani, C. M. Marcus, and P. L. McEuen. Electrical transport in single-wall carbon nanotubes. *Carbon Nanotubes*, 111:455–493, 2008.

[5] M.S. Dresselhaus, G. Dresselhaus, and P. Avouris. *Carbon nanotubes: synthesis, structure, properties, and applications*. Springer, 2001.

[6] S. Sapmaz, P. Jarillo-Herrero, Ya M. Blanter, C. Dekker, and H. S. J. van der Zant. Tunneling in suspended carbon nanotubes assisted by longitudinal phonons. *Physical Review Letters*, 96(2):026801, 2006.

[7] Renaud Leturcq, Christoph Stampfer, Kevin Inderbitzin, Lukas Durrer, Christofer Hierold, Eros Mariani, Maximilian G. Schultz, Felix von Oppen, and Klaus Ensslin. Franck-condon blockade in suspended carbon nanotube quantum dots. *Nat Phys*, 5(5):327–331, 2009.

[8] Sander J. Tans, Michel H. Devoret, Hongjie Dai, Andreas Thess, Richard E. Smalley, L. J. Geerligs, and Cees Dekker. Individual single-wall carbon nanotubes as quantum wires. *Nature*, 386(6624):474–477, 1997.

[9] P. R. Wallace. The band theory of graphite. *Physical Review*, 71(9):622, 1947.

[10] N.W. Ashcroft and N.D. Mermin. *Solid state physics*. Holt, Rinehart and Winston, 1976.

[11] R. Saito, M. Fujita, G. Dresselhaus, and M. S Dresselhaus. *Electronic structure of chiral graphene tubules*, volume 60. AIP, 1992.

[12] Lunhui Guan, Kazu Suenaga, and Sumio Iijima. Smallest carbon nanotube assigned with atomic resolution accuracy. *Nano Letters*, 8(2):459–462, 2008.

[13] Xinjian Zhou. *Carbon Nanotube Transistors, Sensors, and Beyond*. PhD thesis, 2008.

[14] S. Datta. *Electronic transport in mesoscopic systems*. Cambridge University Press, 1997.

[15] Ali Javey, Jing Guo, Qian Wang, Mark Lundstrom, and Hongjie Dai. Ballistic carbon nanotube field-effect transistors. *Nature*, 424(6949):654–657, 2003.

[16] Wenjie Liang, Marc Bockrath, Dolores Bozovic, Jason H. Hafner, M. Tinkham, and Hongkun Park. Fabry - perot interference in a nanotube electron waveguide. *Nature*, 411(6838):665–669, 2001.

[17] K. Grove-Rasmussen, H. I. Jrgensen, and P. E. Lindelof. Fabry-perot interference, kondo effect and coulomb blockade in carbon nanotubes. *Physica E: Low-dimensional Systems and Nanostructures*, 40(1):92–98, 2007.

[18] Wenjie Liang, Marc Bockrath, and Hongkun Park. Transport spectroscopy of chemical nanostructures: The case of metallic single-walled carbon nanotubes. *Annual Review of Physical Chemistry*, 56(1):475–490, 2005.

[19] Jiwoong Park. *Electron transport in single molecule transistors*. PhD thesis, 2003.

[20] C. W. J. Beenakker. Theory of coulomb-blockade oscillations in the conductance of a quantum dot. *Physical Review B*, 44(4):1646, 1991.

[21] Hermann Grabert and Michel H. Devoret. *Single charge tunneling : Coulomb blockade phenomena in nanostructures*. Plenum Press, 1992.

[22] L. P. Kouwenhoven, C. M. Marcus, P. L. Mceuen, S. Tarucha, R. M. Westervelt, and N. S. Wingreen. Electron transport in quantum dots. *Mesoscopic Electron Transport*, 345:105–214, 1997.

[23] Eros Mariani and Felix von Oppen. Electron-vibron coupling in suspended carbon nanotube quantum dots. *Physical Review B*, 80(15):155411, 2009.

[24] Fabio Cavaliere, Eros Mariani, Renaud Leturcq, Christoph Stampfer, and Maura Sassetti. Asymmetric franck-condon factors in suspended carbon nanotube quantum dots. *Physical Review B*, 81(20):201303, 2010.

[25] Stephan Braig and Karsten Flensberg. Vibrational sidebands and dissipative tunneling in molecular transistors. *Physical Review B*, 68(20):205324, 2003.

[26] G. A. Steele, A. K. Httel, B. Witkamp, M. Poot, H. B. Meerwaldt, L. P. Kouwenhoven, and H. S. J. van der Zant. Strong coupling between single-electron tunneling and nanomechanical motion. *Science*, 325(5944):1103–1107, 2009.

[27] O. Usmani, Ya M. Blanter, and Yu V. Nazarov. Strong feedback and current noise in nanoelectromechanical systems. *Physical Review B*, 75(19):195312, 2007.

[28] Andreas K. Huttel, Gary A. Steele, Benoit Witkamp, Menno Poot, Leo P. Kouwenhoven, and Herre S. J. van der Zant. Carbon nanotubes as ultrahigh quality factor mechanical resonators. *Nano Letters*, 9(7):2547–2552, 2009.

[29] Yiming Li, Woong Kim, Yuegang Zhang, Marco Rolandi, Dunwei Wang, and Hongjie Dai. Growth of single-walled carbon nanotubes from discrete catalytic nanoparticles of various sizes. *The Journal of Physical Chemistry B*, 105(46):11424–11431, 2001.

[30] Seong Jun Kang, Coskun Kocabas, Taner Ozel, Moonsub Shim, Ninad Pimparkar, Muhammad A. Alam, Slava V. Rotkin, and John A. Rogers. High-performance electronics using dense, perfectly aligned arrays of single-walled carbon nanotubes. *Nat Nano*, 2(4):230–236, 2007.

[31] Luke Donev. *Carbon Nanotube Transistors: Capacitance Measurements, Localized Damage, And Use As Gold Scaffolding.* PhD thesis, 2009.

[32] H. B. Peng, T. G. Ristroph, G. M. Schurmann, G. M. King, J. Yoon, V. Narayanamurti, and J. A. Golovchenko. Patterned growth of single-walled carbon nanotube arrays from a vapor-deposited fe catalyst. *Applied Physics Letters*, 83(20):4238–4240, 2003.

[33] Zhong Jin, Haibin Chu, Jinyong Wang, Jinxing Hong, Wenchang Tan, and Yan Li. Ultralow feeding gas flow guiding growth of large-scale horizontally aligned single-walled carbon nanotube arrays. *Nano Letters*, 7(7):2073–2079, 2007.

[34] Anne-Claire Dupuis. The catalyst in the ccvd of carbon nanotubes–a review. *Progress in Materials Science*, 50(8):929–961, 2005.

[35] John Cumings, W. Mickelson, and A. Zettl. Simplified synthesis of double-wall carbon nanotubes. *Solid State Communications*, 126(6):359–362, 2003.

[36] Hongkun Park, Andrew K. L. Lim, A. Paul Alivisatos, Jiwoong Park, and Paul L. McEuen. Fabrication of metallic electrodes with nanometer separation by electromigration. 75(2):301–303, 1999.

[37] D. R. Strachan, D. E. Smith, D. E. Johnston, T.-H. Park, Michael J. Therien, D. A. Bonnell, and A. T. Johnson. Controlled fabrication of nanogaps in ambient environment for molecular electronics. 86(4):043109, 2005.

[38] A. A. Houck, J. Labaziewicz, E. K. Chan, J. A. Folk, and I. L. Chuang. Kondo effect in electromigrated gold break junctions. *Nano Letters*, 5(9):1685–1688, 2005.

[39] Chengxiang Xiang, Jung Yun Kim, and Reginald M. Penner. Reconnectable sub-5 nm nanogaps in ultralong gold nanowires. *Nano Letters*, 9(5):2133–2138, 2009.

[40] Hongkun Park, Jiwoong Park, Andrew K. L. Lim, Erik H. Anderson, A. Paul Alivisatos, and Paul L. McEuen. Nanomechanical oscillations in a single-c60 transistor. *Nature*, 407(6800):57–60, 2000.

[41] A. N. Pasupathy, J. Park, C. Chang, A. V. Soldatov, S. Lebedkin, R. C. Bialczak, J. E. Grose, L. A. K. Donev, J. P. Sethna, D. C. Ralph, and P. L. McEuen.

Vibration-assisted electron tunneling in c140 transistors. *Nano Letters*, 5(2):203–207, 2005.

[42] J. J. Parks, A. R. Champagne, T. A. Costi, W. W. Shum, A. N. Pasupathy, E. Neuscamman, S. Flores-Torres, P. S. Cornaglia, A. A. Aligia, C. A. Balseiro, G. K.-L. Chan, H. D. Abrua, and D. C. Ralph. Mechanical control of spin states in spin-1 molecules and the underscreened kondo effect. *Science*, 328(5984):1370–1373, 2010.

[43] J. J. Parks, A. R. Champagne, G. R. Hutchison, S. Flores-Torres, Abru, ntilde, H. D. a, and D. C. Ralph. Tuning the kondo effect with a mechanically controllable break junction. *Physical Review Letters*, 99(2):026601, 2007.